이학박사 학위논문

Ultrafast Non-equilibrium Spectroscopic Investigations on Nematicity of Fe-based Superconductor $Ba(Fe_{1-x}Co_x)_2As_2$

철계초전도체 $Ba(Fe_{1-x}Co_x)_2As_2$의 네마틱 상태에 대한 초고속 비평형 분광학 연구

2020년 2월

서울대학교 대학원

물리 · 천문학부

곽 인 호

Ultrafast Non-equilibrium Spectroscopic Investigations on Nematicity of Fe-based Superconductor $Ba(Fe_{1-x}Co_x)_2As_2$

Inho Kwak

Supervised by
Professor Tae Won Noh

A Dissertation submitted to the Faculty of
Seoul National University
in Partial Fulfillment of the Requirements for
the Degree of Doctor of Philosophy

Feburary 2020

Department of Physics and Astronomy
The Graduate School
Seoul National University

Ultrafast Non-equilibrium Spectroscopic Investigations on Nematicity of Fe-based Superconductor $Ba(Fe_{1-x}Co_x)_2As_2$

철계초전도체 $Ba(Fe_{1-x}Co_x)_2As_2$의 네마틱 상태에 대한 초고속 비평형 분광학 연구

지도교수 노 태 원

이 논문을 이학박사학위논문으로 제출함

2020 년 1 월

서울대학교 대학원

물리천문학부

곽 인 호

곽인호의 박사학위논문을 인준함

2019 년 12 월

위 원 장 박 건 식 (인)

부 위 원 장 노 태 원 (인)

위 원 김 창 영 (인)

위 원 양 범 정 (인)

위 원 김 경 완 (인)

Contents

List of Figures **v**

List of Tables **xvii**

Abstract **xviii**

1 Introduction **1**

1.1 Electronic nematicity in iron-based superconductor 1

1.2 Brief review on previous ultrafast studies on nematicity of Fe-based superconductor 5

1.3 Thesis layout 7

2 Experimental methods **9**

2.1 Sample information 9

2.2 Polarized light microscope and Laue-XRD measurements 11

2.3 Optical pump-probe experimental technique 11

3 Ultrafast polarimetry investigation of the nematic fluctuation in the electron-doped iron pnictide $Ba(Fe_{1-x}Co_x)_2As_2$ **15**

3.1 Introduction 15

3.2 Results and discussions 17

3.2.1 Separating photo-reflectivity into asymmetric and symmetric signals 18

3.2.2 Asymmetric photo-reflectivity due to the B_{2g} nematicity 21

3.2.3 Fit analysis on symmetric photo-reflectivity 24

3.2.4 Quasiparticle dynamics across SDW gap and observations of coherent acoustic wave oscillations 28

3.3 Conclusion 31

4 Measurement of small reflectivity anisotropy in the nematic state and its non-equilibrium dynamics 33

4.1 Introduction 34

4.2 Details of experimental setup 36

4.3 Results and discussions 39

4.3.1 Experimental demonstration of the reflectivity anisotropy in the nematic state 39

4.3.2 Numerical simulation on the reflectivity anisotropy in the nematic state 40

4.3.3 Time-resolved experiment on the reflectivity anisotropy in the nematic state 43

4.4 Conclusion 45

5 Strain-induced rotation of nematic reflectivity anisotropy in electron under-doped $\mathbf{Ba(Fe_{0.955}Co_{0.045})_2As_2}$ 47

5.1 Introduction 47

5.2 Results and discussions 49

5.2.1 Applying uniaxial-strain by affixing the sample to piezo-stack . . . 50
5.2.2 Rotation of C_4 symmetry breaking under uniaxial-strain 50
5.2.3 Applying uniaxial-strain by using piezoelectric-based apparatus . . . 57
5.2.4 Coexistence of B_{2g} and B_{1g} nematicity . . . 60
5.3 Conclusion . . . 62

6 Summary and Concluding Remarks 63

7 References 65

8 Appendix 77

8.1 Effective-temperature model . . . 77
8.2 Estimation of the maximum change of the effective temperature for $Cd_2Os_2O_7$ . . . 80
8.2.1 Homogeneous absorption approximation . . . 80
8.2.2 Exponential absorption & heat propagation approximation along depth . . . 81
8.3 Ultrafast dynamics of a $5d$ pyrochlore antiferromagnet $Cd_2Os_2O_7$ 83
8.4 Optical pump - THz probe spectroscopy setup . . . 88
8.5 Optical pump - THz probe spectroscopy performed at $Ba_{0.6}K_{0.4}BiO_3$ superconducting film . . . 92

9 Publication List 97

9.1 Publications for this thesis 97

9.2 Other publications 98

10 Korean abstract **101**

List of Figures

1.1 Schematic phase diagram of iron pnictide superconductor Ba122-family. 2

2.1 (a) Polarized optical microscope image measured at 30 K and (b) Laue-XRD pattern at 294 K of $Ba(Fe_{0.955}Co_{0.045})_2As_2$ single crystal. (c) Schematic diagram of the twin-domain formation and the detwinned domain in the orthorhombic nematic state. 10

2.2 Schematic diagram and experimental set-up in IBS-CCES of optical pump-probe spectroscopy. This figure has been reproduced with permission from [Lee, 2019] 13

3.1 (a) Probe polarization dependent evolution of the photo-reflectivity of $Ba(Fe_{0.955}Co_{0.045})_2As_2$ single crystal measured as functions of pump-probe delay time τ_d at 30 K below T_{SDW} and T_S. Fluences are set to 120 $\mu J/cm^2$ for pump incidence and 20 $\mu J/cm^2$ for probe incidence. Labels mean angle between the probe polarization and the crystal orientation $[110]_{tetr}$. (b) Asymmetric photo-reflectivity is obtained by Eq. (3.2a) and (c) symmetric photo-reflectivity is obtained by Eq. (3.3a) respectively. (d) Peak values of the asymmetric (circle) and the symmetric (square) photo-reflectivities are measured at $\tau_d = 0.2$ ps as functions of θ. A solid guide line is a simple sinusoidal function of $\Delta R/R \propto \sin(2\theta)$ where θ is the probe polarization. Dashed lines indicate the crystal orientation of $[110]_{tetr}$, parallel to Fe-Fe bonding. 19

3.2 Polarized optical microscope image measured at 30 K, and schematic diagram of the photo-reflectivity measured at the twin-domain region. 20

3.3 Asymmetric photo-reflectivity as functions of delay-time and temperature measured at $Ba(Fe_{1-x}Co_x)_2As_2$ of $x = 0$ %, 4.5 %, 7.5 %, and 8.0 %. Pump fluences are set to 63 $\mu J/cm^2$ for $x = 0$ % in (a), 58 $\mu J/cm^2$ for $x = 4.5$ % in (b), 51 $\mu J/cm^2$ for $x = 7.5$ % in (c), and 52 $\mu J/cm^2$ for $x = 8.0$ % in (d) respectively. 22

3.4 Selected temperature dependent evolutions of the asymmetric photo-reflectivity measured as functions of pump-probe delay time at (a) $x = 0$ %, (b) $x = 4.5$ %, (c) $x = 7.5$ %, and (d) $x = 8.0$ %. All data are normalized by initial peak values at each temperature and at each doping ratio x. 23

3.5 (a) Representative fitting curve using double exponential decay model of Eq. (3.4) and the corresponding experimental data of the asymmetric photo-reflectivity. Fit parameters of (b) constant background, (c)–(d) the fast component, and (e)–(f) the slow component are obtained as functions of temperature. For clarity, amplitudes of A_0, A_1, and A_2 are multiplied by factor two for $x = 7.5$ % and by factor four for $x = 8.0$ % respectively. 25

3.6 Symmetric photo-reflectivity as functions of delay-time and temperature measured at $Ba(Fe_{1-x}Co_x)_2As_2$ of $x = 0$ %, 4.5 %, 7.5 %, and 8.0 %. Pump fluences are set to 63 $\mu J/cm^2$ for $x = 0$ % in (a), 58 $\mu J/cm^2$ for $x = 4.5$ % in (b), 51 $\mu J/cm^2$ for $x = 7.5$ % in (c), and 52 $\mu J/cm^2$ for $x = 8.0$ % in (d) respectively. . . 26

3.7 (a)–(b) Representative fitting to experimental data of the symmetric photo-reflectivity using Eq. (3.5). Obtained fit parameters (c)–(d) for electronic relaxation, (e)–(g) for acoustic wave oscillation, and (h) for constant background as functions of temperature. 27

3.8 (a) Amplitudes of the fast asymmetric relaxation component A_1 and of the sub-ps symmetric relaxation component B_e. (b) Relaxation time of the fast asymmetric relaxation component τ_1 and of the sub-ps symmetric relaxation component τ_e. Asymmetric fit parameters of A_1 and τ_1 are obtained by fit analysis using Eq. (3.4). Symmetric fit parameters of B_e and τ_e are obtained by fit analysis using Eq. (3.5). Solid guide lines are generated by using Eq. (6) for amplitudes and Eq. (28) for relaxation times in Ref. [Kabanov et al., 1999] as described in main text. 29

3.9 Temperature dependent evolutions of the coherent acoustic wave oscillation in the symmetric photo-reflectivity. Experimental data (open circles) are well fitted to solid fitting lines of Eq. (3.5). For clarity, each data is shifted by an interval of 2×10^{-4}. . . 30

4.1 Schematic diagram of the experimental setup. Ultrafast pulse is split into pump and probe beams after a beam splitter (B.S.). Optic axis of PEM is set to be 45° with respect to the incoming probe polarization. After the PEM, the probe polarization is varied by rotating half wave-plate. 37

4.2 Experimental geometry of the sample and the probe polarization, and experimental results on $Ba(Fe_{0.955}Co_{0.045})_2As_2$ single crystals. (a) The orientations of the probe polarization θ and of the crystal axis ϕ are shown with respect to the plane of incidence. In the experiment, the angle of incidence α is 10°. The 2ω lock-in signal $R_{2\omega}/R$ is shown for the cases of (b) $\phi = 45°$ and (c) $\phi = 0°$. Data measured in the nematic state at 50 K (blue open triangles) and in the normal state at 294 K (red open circles) are vertically shifted for clarity. Black open squares are obtained by subtracting data at 294 K from data at 50 K. . . . 38

4.3 Simulations of the reflectivity anisotropy. (a) Comparison of the experimentally obtained nematic anisotropy (open square) with simulated ones for $\alpha = 10°$ and $\phi = 0°$ by Eq. (4.6) and Eq. (4.7). All of them agree with the the exact case of $\alpha = 0°$ at $\phi = 0°$ (symbol $\times$). (b) Nematic anisotropy simulated for various values of α by Eq. (4.6). (c) The simulated nematic anisotropy is normalized by the normal incidence case. η is a relative ratio of a half of birefringence $\delta n/2$ to the refractive index of the isotropic case n_{ab}. Refractive index n_a and n_b for the nematic state is varied as described in the text. 41

4.4 Pump-probe results of the reflectivity anisotropy. (a) Nematic anisotropy $\delta R/R$ of $Ba(Fe_{0.955}Co_{0.045})_2As_2$ single crystal at 50 K obtained by Eq. (4.3) and (b) its transient change $\Delta(\delta R)/R$ measured at various delay times τ_d. The pump fluence is fixed at 31 μJ/cm^2. 44

5.1 Strain dependent experiment on the photo-reflectivity performed at $Ba(Fe_{0.955}Co_{0.045})_2As_2$ single crystals. Experimental schematics (a) of the isotropic strain condition and (d) of the uniaxial-strain condition. Probe polarization dependent evolution of the photo-reflectivity $\Delta R/R$ is measured at 30 K as a function of delay time τ_d (b) under isotropic strain and (e) under uniaxial-strain. The polling axis of the piezo-stack is aligned to be parallel to $[110]_{tetr}$ crystal orientation. Polar axis plot of the photo-reflectivity measured at $\tau_d = 0.2$ ps as a function of the probe polarization (c) under isotropic strain and (f) under uniaxial-strain. Fluences are set to be 120 μJ/cm^2 for the incident pump and 20 μJ/cm^2 for the incident probe at the experiment under the isotropic strain, and 39 μJ/cm^2 for the incident pump and 1.2 μJ/cm^2 for the incident probe under the uniaxial-strain. . 51

5.2 Reflectivity anisotropy of $Ba(Fe_{0.955}Co_{0.045})_2As_2$ is measured at 30 K under uniaxial-strain along $[110]_{tetr}$ using the method discussed in Chapter 4. The result is normalized by the maximum value of equilibrium anisotropy measured without pumping. (a) Reflectivity anisotropy $\delta R/|\delta R|^{eq}_{Max}$ measured as functions of θ in equilibrium state without pumping (blue solid line) and in non-equilibrium state at $\tau_d = 0.2$ ps (red solid line). The incident probe polarizations of $\theta = 0°$ and $\theta = 90°$ are parallel to the Fe-Fe bonding directions. (b) Time-transient reflectivity anisotropy $\delta R/|\delta R|^{eq}_{Max}$ as a function of delay time τ_d measured at the incident probe polarization of $\theta = 69°$. A dashed vertical line indicates $\tau_d = 0.2$ ps. 54

5.3 (a) Transient anisotropy change normalized by equilibrium anisotropy $\Delta(\delta R)/|\delta R|^{\rm eq}_{\rm Max}$ measured as a function of the incident probe polarization θ and the delay time τ_d at 30 K under uniaxial-strain. Incident fluences are set to be 41 μJ/cm^2 for pump and 5 μJ/cm^2 for probe. (b) Transient anisotropy change $\Delta(\delta R)/R$ measured as functions of the incident probe polarization at $\tau_d = 0.2$ ps with incident pump fluences of 41 μJ/cm^2 (blue solid line) and 1,000 μJ/cm^2 (red dashed line) respectively. They are normalized to the maximum values at each fluence conditions respectively. (c) Normalized transient anisotropy change by equilibrium anisotropy $|\Delta(\delta R)|_{\rm Max}/|\delta R|^{\rm eq}_{\rm Max}$ measured as a function of incident pump fluence. Isotropic-strain result (open circle) is obtained from difference between the maximum and the minimum values of the photo-reflectivity $\Delta R_{\rm Max} - \Delta R_{\rm Min}$ in Fig. 5.1(c). It is scaled to fit to the uniaxial-strain result (open square). A grey solid guide line is a simple saturation function of $|\Delta(\delta R)|_{\rm Max}/|\delta R|_{\rm Max} = A\left(1 - e^{-\Phi_{\rm sat}/\Phi}\right)$ where Φ is the incident pump fluence, $\Phi_{\rm sat} = 59$ μJ/cm^2, and $A = 0.77$. . 56

5.4 (a) Schematic diagram of time-resolved reflectivity anisotropy measurement on $Ba(Fe_{0.955}Co_{0045})_2As_2$ under uniaxial strain. The sample is affixed to the piezoelectric-based apparatus with silver-epoxy and torr-seal. Tensile-strain is applied along [110]tetr crystal orientation by applying DC voltage. (b) Equilibrium anisotropy $\delta R/R$ and (c) transient anisotropy $\Delta(\delta R)/R$ measured as functions of the incident probe polarization at 30 K with 0 V and 150 V DC voltage applied on the side piezoelectric stacks. The difference between 0 V and 150 V is displayed below panels respectively. The incident probe polarization of 0° is parallel to the crystal orientation of [110]tetr. Fluences are set to be 41 $\mu J/cm^2$ for pump and 5 $\mu J/cm^2$ for probe. 58

5.5 Polar axis plots of the numerically simulated sinusoidal functions. The red and blue colors indicate the positive and the negative signs respectively. The phase shift by 22.5° in the middle plot is simply obtained from average of the B2g symmetry (left) and the B1g symmetry (right). 59

8.1 Schematic diagrams of the relaxation dynamics in terms of the effective-temperatures of the subsystems. Colored lines indicate the effective-temperature changes of the electron (solid line), spin (filled dashed line), strongly coupled phonon (SCP, open dashed line), and total lattice (dotted line) subsystems. This figure has been reproduced from [Kwak et al., 2019a]. 77

8.2 (a) Temperature distribution function $T_L(z, \tau_d)$ at 100 nm and 20 ns window. (b) Lattice temperature change distribution $\Delta T_L(z, \tau_d)$ at various time delay τ_d. (c) The lattice temperature change distribution $\Delta T_L(z, \tau_d)$ integrated over the depth. This figure has been reproduced from [Kwak et al., 2019a]. 83

8.3 Photo-reflectivity $\Delta R/R$ in two temporal windows, spanning -0.5 – 4 ps (left panel), and 4 – 1,800 ps (right panel) over temperatures from 146 K to 233 K. This figure has been reproduced from [Kwak et al., 2019a]. 84

8.4 (Color online) Temperature-dependent evolution of $\Delta R/R$ (circles) measured at $t_d = 1.8$ ns and $(\partial R_{\mathrm{eq}}/\partial T)/R_{\mathrm{eq}}$ (squares) obtained from the equilibrium reflectivity R_{eq}. Inset: The R_{eq} at 1.55 eV measured by spectroscopic ellipsometry at 20 K intervals from 100 to 200 K, and at 1 K intervals from 200 to 235 K. This figure has been reproduced from [Kwak et al., 2019a]. 86

8.5 Schematic diagram of experimental set-up for optical pump - THz probe spectroscopy. This figure has been reproduced with the permission of [Lee, 2019]. 88

8.6 Generation and detection mechanism of THz lights by using second harmonic effects. This figure has been reproduced with permission of [Lee, 2019] 89

8.7 THz spectra obtained with the home-made THz spectroscopy equipment in IBS-CCES. 90

8.8 Demonstration of THz spectra tuning by rotating GaSe nonlinear crystal of 60 μm thickness. This varies the angle of incidence of the generation beam and, therefore, the phase-matching condition changes. Note that the pulse duration of the generation beam is about 40 fs FWHM and bandwidth is 30 nm FWHM at 800 nm center frequency. 91

8.9 THz time-domain spectroscopy on the best quality $Ba_{0.6}K_{0.4}BiO_3$ superconducting film. Thickness of the film on a MgO substrate is 100 nm. Transmission spectra are measured at various temperature. Superconducting response is clearly observed in transmission spectra. The overall trend of T_S/T_N is understood by a single isotropic BCS gap dynamics. Thick solid lines are generated by simulation on transmission ratio with a single isotropic BCS gap [Zimmermann et al., 1991] using $T_C = 18$ K, $\Delta(0) = 3.43$ meV, and $\sigma_{\rm DC} = 950\ \Omega^{-1}{\rm cm}^{-1}$. 93

8.10 THz time-domain spectroscopy on a degraded $Ba_{0.6}K_{0.4}BiO_3$ superconducting film. Thickness of the film on a MgO substrate is 100 nm. Transmission spectra are measured at various temperature. The measured transmittivity spectra is not explained by isotropic single gap feature. Onset plot in a right panel exhibits the magnetic susceptibility data χ_m as a function of temperature. Broad transition in χ_m may be explained by continuous distribution of different $\Delta_{\rm SC}$ size. 94

8.11 Optical-pump and THz-probe spectroscopy is performed on the degraded $Ba_{0.6}K_{0.4}BiO_3$ superconducting film performed at 11.7 K with 0.69 $\mu J/cm^2$ pump fluence. Fast relaxation is clearly observed in the transient change of transmission phase $\Delta\theta_T$. Pump induced signal results from phase change in THz electric field. It is consistent to temperature dependent evolution of the equilibrium transmission. 95

8.12 Fluence dependent optical-pump and THz-probe spectroscopy on the degraded $Ba_{0.6}K_{0.4}BiO_3$ superconducting film performed at 11.7 K with fixed probe delay where the change in the electricfield ΔE is the maximum. Phonon bottleneck process is dominant below 1 $\mu J/cm^2$ pump fluence. Above that, bi-particle recombination becomes dominant. Full depletion of SC state by the optical pump is observed at 2 $\mu J/cm^2$ pump fluence, fairly small value compared to other conventional superconductors [Demsar et al., 2003, Beck et al., 2011]. 96

List of Tables

2.1 List of transition temperatures of $Ba(Fe_{1-x}Co_x)_2As_2$ single crystals used in this thesis research 9

2.2 Detailed specification of optical pump-probe spectroscopic system in IBS-CCES 12

ABSTRACT

Ultrafast Non-equilibrium Spectroscopic Investigations on Nematicity of Fe-based Superconductor $Ba(Fe_{1-x}Co_x)_2As_2$

Inho Kwak
Department of Physics and Astronomy
The Graudate School Seoul National University

This thesis comprises researches of near-infrared polarimetry pump-probe experiments on the electronic nematicity of $Ba(Fe_{1-x}Co_x)_2As_2$, which has attracted enormous interest in the relation to the high T_C superconductivity.

Optical pump-probe reflectometry are performed at $Ba(Fe_{1-x}Co_x)_2As_2$ single crystals over $x = 0$ %, 4.5 %, 7.5 %, and 8.0 %. The measured photo-reflectivity are split into asymmetric and symmetric photo-reflectivities. Detailed temperature-dependent evolution of the asymmetric photo-reflectivity confirms that the B_{2g} nematic fluctuation strongly survives even without the orthorhombic lattice distortion. Quasiparticle dynamics across the spin-density-wave gap is observed in a picosecond timescale relaxation and coherent acoustic wave oscillation is dephased in a few tens of picosecond timescale. These observations suggest that the asymmetric photo-reflectivity successfully

features the spin-nematic fluctuation in a picosecond timescale and the lattice-nematic fluctuation with tens of picosecond timescale.

Measuring the small optical anisotropy in the nematic phase is usually hindered by the geometric anisotropy due to the finite angle of incidence, differentiating the reflectivities between s- and p-polarizations. I present a new experimental method to investigate nematic anisotropy and its non-equilibrium dynamics. As a demonstration, the nematic reflectivity anisotropy is measured at $Ba(Fe_{0.955}Co_{0.045})_2As_2$ single crystal, which has the B_{2g} nematic phase. Numerical simulations confirm that our method is highly reliable in conventional experimental condition. In addition to this, our method is used for time-resolved experiment of nematic anisotropy which confirms that ultrafast photo-excitation suppresses the nematic order.

Finally, I present strain-dependent reflectometry pump-probe experiment on electron doped $Ba(Fe_{0.955}Co_{0.045})_2As_2$, which shows a typical B_{2g} nematicity with an antiferromagnetic order in an orthorhombic crystal structure. Uniaxial external pressure has usually been used to obtain a single nematic domain. However, the photo-reflectivity measured under uniaxial-strain along $[110]_{\mathrm{tetr}}$ reveals an unexpected nematicity of which C_4 symmetry breaking orientation is rotated by 20°. Successive reflectivity anisotropy measurements on the equilibrium state confirm that the peculiar rotation by about 20° is induced by the uniaxial-strain. Our observation suggests the microscopic coexistence of the B_{2g} and B_{1g} nematicity under the uniaxial strain in the electron-doped iron pnictide.

Key words: Ultrafast spectroscopy, Pump-probe spectroscopy, Strongly correlated electron systems, Superconductivity, Fe-based superconductor, Electronic nematicity, Uniaxial strain

Student number: 2014-21355

1. Introduction

1.1 Electronic nematicity in iron-based superconductor

Electronic nematicity has created a great deal of interest in relation to the unconventional superconductivity. During the recent decade, the nematic phases have been found to precede the superconductivity in numerous correlated electronic systems. In the cuprate, the rotational symmetry breaking due to the nematicity is observed in the pseudogap state [Daou et al., 2010,Sato et al., 2017]. In the heavy-Fermion material, the hidden ordered phase, discovered above the superconductivity, was found to be the electronic nematic phase [Okazaki et al., 2011, Riggs et al., 2015, Ronning et al., 2017]. In topological superconductor $Sr_xBi_2Se_3$, the rotational symmetry breaking is revealed above the superconducting transition temperature [Sun et al., 2019]. Most of iron pnictide share a common feature that the superconductivity emerges as the nematicity is suppressed by chemical doping, pressure, or magnetic fields [Paglione and Greene, 2010, Chubukov, 2012, Keimer et al., 2015, Si and Steglich, 2010]. These findings suggest that extensive investigations of the nematic phase is essential for understanding both the intrinsic physical properties and the superconductivity of the correlated electronic systems.

In iron based superconductors, the static nematic order is accompanied with the structural transition from the tetragonal lattice of C_4 symmetry to the orthorhombic lattice of B_{2g} symmetry as displayed in Fig. 1.1. However,

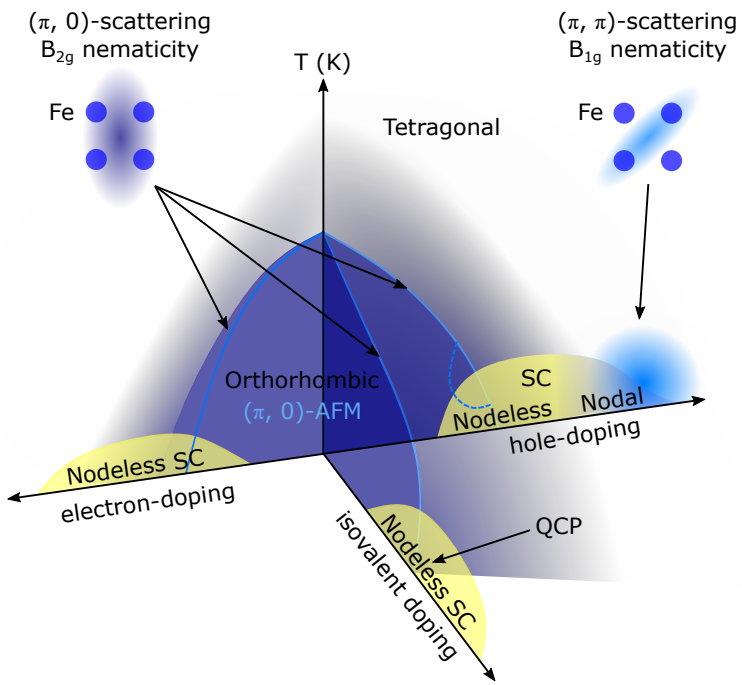

Figure 1.1: Schematic phase diagram of iron pnictide superconductor Ba122-family.

various experimental investigations have revealed the evidences of the electronic nematicity without lattice C_4 symmetry breaking [Kasahara et al., , Yi et al., 2011, Yi et al., 2014, Kuo et al., 2016]. Furthermore, extensive studies have discovered the non-Fermi liquid behaviors in the vicinity of the superconducting dome, suggesting the nematic quantum criticality [Shibauchi et al., 2014, Kuo et al., 2016, Liu et al., 2016, Hosoi et al., 2016]. The quantum fluctuations, expected at the quantum critical point, is supposed to provide the pairing interaction for the high-T_C superconductivity. In addition to this, recent studies of heavily hole-doped material $(Ba_{1-x}Rb_x)_2Fe_2As_2$ have discov-

ered another nematic phase of B_{1g} symmetry, whose principal axis is rotated by 45 degrees from the Fe-Fe bonding direction [Liu et al., 2019, Ishida et al., 2019]. The B_{1g} nematic state is accompanied with the nodal superconductivity while the B_{2g} nematic state of the moderately doped materials is in the vicinity of the nodeless superconductivity as displayed in Fig. 1.1. These findings consistently imply the close relation between the iron-based superconductivity and the electronic nematicity.

Spin and orbital instabilities are the potential candidates for the leading order parameter which drives the electronic nematicity. The electronic nematicity is manipulated by interplay between charge, spin, orbital, and lattice degrees of freedom. In most of iron-based materials, the nematic phase is followed by the spin-density-wave (SDW) order where Fe-3d spins are aligned ferromagnetically along shorter Fe-Fe bonding direction and antiferromagnetically along longer direction respectively. Magneto-torque measurement and Raman scattering measurement reported that the strong spin fluctuations are accompanied with the electronic nematicity [Kasahara et al., , Kretzschmar et al., 2016]. On the other hand, the nematic phase is highly related to orbital anisotropy. Various experiments using X-ray have revealed the strong orbital fluctuations in the vicinity with the nematic phase [Kim et al., 2013, Yi et al., 2011, Yi et al., 2014, Gallais et al., 2013, Gallais and Paul, 2016, Kretzschmar et al., 2016]. Therefore, the origin of the nematicity is still under controversial and further investigations are required to find out a genuine leading order of the nematicity.

Uniaxial-strain have been employed to detwin single crystals in numerous investigations of the nematic phase. The orthorhombic phase transition introduces stripe-type twin-domains to the crystal in the B_{2g} nematic state. The small domain width of a few micrometers makes it challenging to investigate the intrinsic nematic properties. Therefore, most of experiments on the anisotropic electronic properties in the B_{2g} nematic state have been performed at detwinned sample exhibiting a large enough single domain under the uniaxial-strain [Tanatar et al., 2010, Chu et al., 2010, Yi et al., 2011, Kasahara et al., , Nakajima et al., 2012, Kim et al., 2013, He et al., 2017, Pfau et al., 2019, Huh et al., 2019].

The uniaxial-strain also introduce the conjugate field to the nematic order parameter. The strain-induced conjugate field have been used to measure elastoresistivity tensor, expected to be proportional to the nematic susceptibility [Kuo et al., 2013, Shapiro et al., 2016, Kuo et al., 2016]. However, the first principle calculations show that the Fermi-surface of the iron pnictide is easily modulated by the uniaxial-strain [Tomić et al., 2012, Tomić et al., 2013]. Recent experimental studies have also revealed that uniaxial-strain can be a tuning parameter for the superconductivity as well as the nematic and the long-range magnetic order in iron pnictide [Tam et al., 2017, Ikeda et al., 2018, Willa et al., 2019, Malinowski et al., 2019]. Therefore, the influence of the applied strain needs to be carefully considered.

1.2 Brief review on previous ultrafast studies on nematicity of Fe-based superconductor

Ultrafast pump-probe study provides a unique opportunity to investigate the nematic order, manipulated by the complex interplay between charge, spin, orbital, and lattice degrees of freedom in iron-based materials. Extensive time-resolved experiments have revealed the strong coupling between the electronic structure and the lattice modulation, which should affect the spin-density-wave, nematic, and superconducting orders [Kim et al., 2012, Gerber et al., 2015, Gerber et al., 2017]. In particular, optical-pump and THz-probe spectroscopy have shown that the spin-density-wave order can be transiently induced by the coherent lattice vibration due to the ultrafast photo-excitation [Kim et al., 2012]. A time-resolved polarimetry investigation of iron pnictide have distinguished the spin contribution to the static nematic order from the magnetic contribution with distinct timescales [Patz et al., 2014].

Ultrafast optical pump-probe reflectometry provides relatively small spot size and a great signal-to-noise ratio, which make it possible to measure the anisotropic electronic response even without uniaxial-strain. Indeed, the photo-reflectivity have been measured at various Fe-based materials without any external pressure and clearly features the broken four-fold symmetry due to the nematicity [Stojchevska et al., 2012,Luo et al., 2017,Liu et al., 2018,Thewalt et al., 2018]. On the other hand, strain dependent pump-probe investigations have been barely performed at the iron based materials. As long as I know, there exist only one report [Thewalt et al., 2018], regardless of the

recent interesting reports on the possibility of the uniaxial-strain as a tuning parameter.

1.3 Thesis layout

In Chapter 2, I describe the details of optical pump-probe polarimetry experiments to investigate non-equilibrium dynamics of $Ba(Fe_{1-x}Co_x)_2As_2$ single crystals.

In Chapter 3, I will present results of optical pump-probe polarimetry investigations on $Ba(Fe_{1-x}Co_x)_2As_2$ single crystals of $x = 0$ %, 4.5 %, 7.5 %, and 8.0 %. Temperature-dependent evolutions of the measured photo-reflectivity suggest the presence of two distinctive contributions to the nematic fluctuations without lattice C_4 symmetry breaking. They are clearly distinguished by distinctive time-scales.

In Chapter 4, I will describe a new experimental method using photo-elastic-modulator (PEM) to investigate small reflectivity anisotropy. This method is employed in Chapter 5 to measure the reflectivity anisotropy in the nematic state without ultrafast pumping. The result does demonstrate that ultrafast photo-excitation simply suppresses the reflectivity anisotropy by melting the static nematic order.

In Chapter 5, I will present results of strain-dependent optical pump-probe polarimetry on electron-doped $Ba(Fe_{0.955}Co_{0.045})_2As_2$. The result suggests that the uniaxial-strain introduces the Ising-like nematic state where the B_{2g} nematicity and the B_{1g} nematicity are comparable.

2. Experimental methods

In this chapter, I describe the details of optical pump-probe experimental technique and sample information of $Ba(Fe_{1-x}Co_x)_2As_2$ single crystals used in this thesis research.

2.1 Sample information

High quality single crystals of $Ba(Fe_{1-x}Co_x)_2As_2$ of x = 0 %, 4.5 %, 7.5 %, and 8.0 % were grown by a self-flux method. Transition temperatures of structure (T_S), SDW order (T_{SDW}), and superconductivity (T_C) are summarized in Table 2.1. In high temperature, the crystals have tetragonal lattice structure, whose principal axes of $[100]_{\mathrm{tetr}}$ and $[010]_{\mathrm{tetr}}$ are diagonal to the Fe-Fe bonding directions. As temperature decreases down below T_S, the structure transition occurs from tetragonal lattice to the orthorhombic lattice, whose principal axes of $[100]_{\mathrm{orth}}$ and $[010]_{\mathrm{orth}}$ are parallel to the Fe-Fe bonding directions. Below T_{SDW}, the Fe-3d spin moments are aligned antiferromagnetically along a direction of longer axis and ferromagnetically along a direction of shorter axis.

Cobalt ratio x	T_S	T_{SDW}	T_C
0 %	134 K	134 K	-
4.5 %	75 K	60 K	14 K
7.5 %	-	-	24.1 K
8.0 %	-	-	21 K

Table 2.1: List of transition temperatures of $Ba(Fe_{1-x}Co_x)_2As_2$ single crystals used in this thesis research

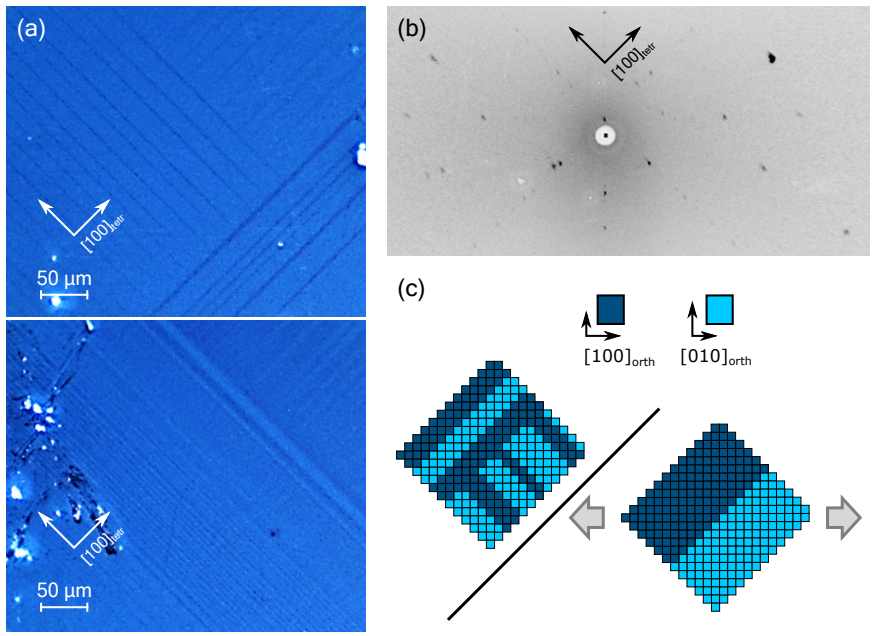

Figure 2.1: (a) Polarized optical microscope image measured at 30 K and (b) Laue-XRD pattern at 294 K of $Ba(Fe_{0.955}Co_{0.045})_2As_2$ single crystal. (c) Schematic diagram of the twin-domain formation and the detwinned domain in the orthorhombic nematic state.

To minimize unintentional strain effect, the samples are affixed with GE-Varnish to Cu-plate. In preparing spectroscopic experiments, the samples are cleaved in ambient condition and then immediately transferred to an optical cryostat (MicrostatHires2 or MicrostatHe2, Oxford Instruments) to minimize degradation effect.

2.2 Polarized light microscope and Laue-XRD measurements

The samples in the orthorhombic nematic state exhibit twin domain structure. Polarized light microscope measurement is performed to verify the formation of the twin domain structure. The sample is illuminated by linearly polarized light, and the reflected light is collected after the crossed polarizer. Therefore, the microscopic image is obtained only when the polarization of the reflected light is rotated by anisotropic response due to the nematic order. Introducing a compensator into the incidence or reflected beam make the colors of neighboring domains different.

Polarized light microscopic image measured at the cleaved surface of $x = 4.5$ % $Ba(Fe_{1-x}Co_x)_2As_2$ single crystal clearly exhibits the stripe-type pattern below T_S as displayed in Fig. 2.1(a). Orientation of the twin boundary is diagonal to the orthorhombic axis of $[110]_{\mathrm{tetr}}$, identified by Laue-XRD measurement as displayed in Fig. 2.1(b). We note that widths of the alternative brighter and darker regions show considerable variations from a few micron to a few tens of microns depending on the spatial location.

2.3 Optical pump-probe experimental technique

For optical pump-probe experiments, I used a Ti:sapphire oscillator (Vitara-T, Coherent Co.) and a re-generative amplifying system (RegA 9040, Coherent Co.). The oscillator initially generates pulse of 1.55 eV photon energy and of a

Equipment	*model* (*company*)	*specification*
Oscillator	Vitara-T (Coherent)	1.55 eV, 15 fs, 80 MHz
Amplifier	RegA9040 (Coherent)	1.55 eV, 40 fs, 250 kHz
Lock-in amplifier	SR830 (SRS).	
Balanced detector	Nirvana2007 (Newport)	
Optical cryostat	MicroHiRes2 (Oxford)	temperature: 4-400 K
	MicroHe2 (Oxford)	temperature: 4-400 K
Linear stage	M-IMS600LM (Newport)	repeatability: ± 0.09 μm

Table 2.2: Detailed specification of optical pump-probe spectroscopic system in IBS-CCES

pulse duration of $\sim$ 15 fs full width at half maximum (FWHM) with 80 MHz repetition rate. The generated ultrashort pulse is amplified to 6 uJ per pulse with 250 kHz repetition rate. The amplified pulse is linearly polarized to be parallel to the optic table with 500:1 contrast ratio. Final pulse duration at the location of sample is minimized by a folded grating compressor to be lower than 40 fs FWHM. Bandwidth is 30 nm FWHM at 800 nm center wavelength, where the penetration depth is about 25 nm measured by ellipsometer on $BaFe_2As_2$ single crystal.

The amplified pulse is split into pump and probe beams, and then they reaches to the sample surface passing through different optical paths as displayed in Fig. 2.2. Length of pump optical path is varied by using a motorized linear stage (M-IMS600LM, Newport Co.) to modulate delay time τ_d, the interval between the pump arriving time and the probe arriving time to the sample. The motorized linear stage provides the uni-directional repeatability of 0.09 μm, corresponding to a delay time resolution of 0.6 fs and the maximum travel length of 600 mm, corresponding to a delay time window of 4

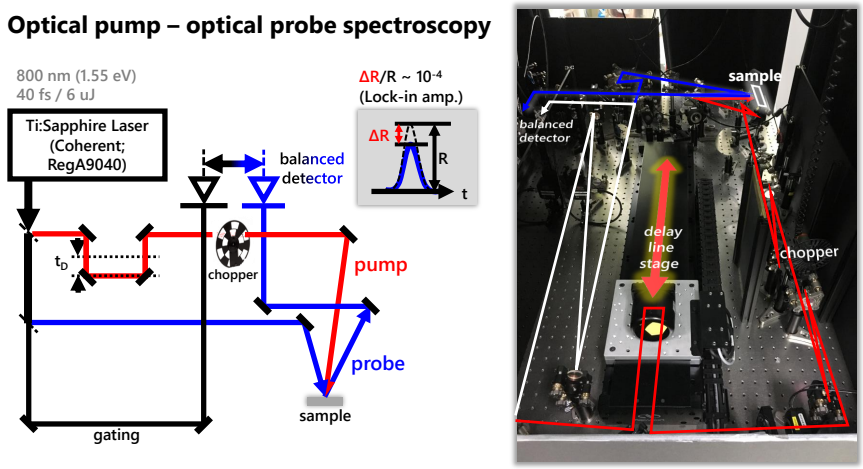

Figure 2.2: Schematic diagram and experimental set-up in IBS-CCES of optical pump-probe spectroscopy. This figure has been reproduced with permission from [Lee, 2019]

ns.

Both of the pump and the probe beams are focused on the cleaved sample surface with spot sizes of 100 μm FWHM for the pump and 50 μm FWHM for the probe. In focusing beams, concave mirrors are used of 500 mm focal length for the pump and of 250 mm focal length for the probe to minimize high-order dispersion of group velocity. Pump and probe fluences are varied by rotating neutral density filters. The probe fluence was confirmed to be in the linear response region.

Photo-excitation by the pump induces transient change in the electronic structure of materials by exciting electrons in the occupied state to the unoccupied state. Recovery process of the photo-excited carriers is monitored by measuring the probe intensity after reflection from the sample. The reflected

probe intensity is measured with a balanced detector (Nirvana, Newport Co.) and its transient change by the pump is amplified through a lock-in amplifier (SR830, Stanford Research Systems) with a optical chopper modulating the pump beam with 2.3 kHz frequency. The amplified transient change is normalized by the reflected probe intensity and the photo-reflectivity $\Delta R/R$ is obtained with the extremely small noise level of $\sim 2 \times 10^{-5}$.

For polarimetry investigation of the electronic nematicity, orientation of the probe polarization is varied by using a half wave plate located just before the concave mirror at the probe branch. For a precise control, the half wave plate is mounted on a motorized rotation stage (Conex-AG-PR100P, Newport Co.), providing an on-axis accuracy of 80 mdeg. I note that variation of the pump polarization orientation does not give rise to any change for all of the results described in this thesis research. Therefore, the orientation of the pump polarization is set to be parallel to the plane of incidence to minimize the scattering effect.

Table 2.2 lists models and manufacturing companies of equipment used in this thesis research.

3. Ultrafast polarimetry investigation of the nematic fluctuation in the electron-doped iron pnictide $\mathbf{Ba(Fe_{1-x}Co_x)_2As_2}$

In this chapter I present near-infrared pump-probe polarimetry investigations of the nematic fluctuations in the electron-doped $Ba(Fe_{1-x}Co_x)_2As_2$ single crystals with $x = 0$ %, 4.5 %, 7.5 %, and 8.0 %. The measured photo-reflectivity are split into asymmetric response and symmetric response. The asymmetric photo-reflectivity measured as functions of the probe polarization clearly exhibits four-fold symmetry due to the electronic nematicity. The asymmetric photo-reflectivity is recovered by two relaxation processes: a fast relaxation and a slow relaxation. Detailed temperature-dependent evolutions and fit analysis of the asymmetric photo-reflectivity will be discussed.

3.1 Introduction

Electronic nematicity is manipulated by the complex interplay between the charge, spin, orbital, and lattice degrees of freedom. In iron based materials, the static nematic order is accompanied with the lattice C_4 symmetry breaking. However, it has been observed that rotational symmetry breaking of the electronic structure can occur even without lattice symmetry breaking, implying the electronic origin for the nematicity. The unusually strong nematic fluctuations have been revealed by numerous experimental studies on

isotropic tetragonal phase [Kasahara et al., , Kim et al., 2013, Kretzschmar et al., 2016, Thewalt et al., 2018]. Furthermore, extensive studies on the nematic fluctuations have suggested the quantum critical point in the vicinity of the superconducting dome [Shibauchi et al., 2014, Kuo et al., 2016, Liu et al., 2016, Hosoi et al., 2016]. Therefore, the electronic nematicity has been one of the potential candidates for the bosonic glue of the high-T_C superconductivity.

Origin of nematicity in iron-based materials is still controversial. In most of iron pnictide, nematic phase precedes the spin-density-wave (SDW) order of ferro-/antiferro-type Fe-3d spin alignment along shorter/longer Fe-Fe bonding directions, implying fluctuation of spin moment plays an important role for the nematicity. On the other hand, the long-range order of the magnetic moment is absent in iron chalcogenide such as FeSe systems, one of the most famous Fe-based superconductors. Therefore, orbital degree of freedom has been expected to drive the nematicity in iron chalcogenide [Beak et al., 2015].

Ultrafast pump-probe measurement provides a unique opportunity to investigate the interplay between charge, spin, orbital, and lattice degrees of freedom. State-of-the-art time-resolved experiments have revealed the strong influence of the coherent lattice vibration due to the A_{1g} phonon mode on the electronic state of the SDW, nematic, and superconducting orders [Kim et al., 2012, Gerber et al., 2015, Gerber et al., 2017]. Time-resolved polarimetry investigation of iron pnictide has successfully distinguished nematic fluctuations of the structural and magnetic origins based on their distinct relaxation timescales [Patz et al., 2014]. However, most of investigations have employed

a few tens of micrometers or larger spot size of probe beam, much larger than the stripe-type twin domain width of a few micrometers [Stojchevska et al., 2012, Luo et al., 2017, Liu et al., 2018, Thewalt et al., 2018]. Therefore, more systematic investigations are required for understanding its non-equilibrium dynamics.

In following sections, I will present near-infrared pump-probe experiments of the electron-doped $Ba(Fe_{1-x}Co_x)_2As_2$ single crystals with $x = 0$ %, 4.5 %, 7.5 %, and 8.0 %. The measured photo-reflectivity are consisting of symmetric response independent on the probe polarization and asymmetric response dependent on the probe polarization. Results of detailed temperature-dependent experiments and fit analysis will be discussed.

3.2 Results and discussions

The photo-reflectivity is measured as a function of pump-probe delay time τ_d. For pump-probe experiment, we use a Ti:sapphire regenerative amplifier system, which generates pulses of 40 fs duration and 1.55 eV photon energy at 250 kHz repetition rate. The generated pulse was split into pump and probe beams and focused on a cleaved surface of the sample with 100 μm for pump and 50 μm for probe spot sizes (full width at half maximum) respectively. The pump and probe fluence were varied by rotating a neutral density filter and indicated in each figure caption. The probe fluence was confirmed to be in the linear response region. The probe polarization was varied by rotating a

half wave plate located in front of the sample. We set the pump polarization parallel to the plane of incidence because the result does not depend on the pump polarization.

3.2.1 Separating photo-reflectivity into asymmetric and symmetric signals

The photo-reflectivity highly depends on the orientation of the probe polarization in the nematic state. Figure 3.1(a) displays the representative photo-reflectivity of $Ba(Fe_{0.955}Co_{0.045})_2As_2$ measured at 30 K below T_{SDW} and T_S. Ultrafast pumping introduces a peak structure by melting both the nematic order and the SDW order. Therefore, the peak value is sensitive to the probe polarization and exhibits the extremes whenever the probe polarization is parallel to the crystal orientation of $[110]_{\mathrm{tetr}}$.

The peak value of the photo-reflectivity does depend on the measuring position in the sample surface. The probing spot is larger than typical width of twin-domain, whose area contrast gradually varies depending on the measuring position as displayed in Fig. 2.1(a). Therefore, the measured photo-reflectivity is an averaged signal of the alternatively adjacent two kinds of domains, whose orthorhombic principal axes are rotated by 90 degrees each other as displayed in Fig. 3.2:

$$\begin{aligned}\Delta R(\theta) = p\left(\Delta R_a \cos^2\theta + \Delta R_b \sin^2\theta\right) \\ + (1-p)\left(\Delta R_b \cos^2\theta + \Delta R_a \sin^2\theta\right),\end{aligned} \tag{3.1}$$

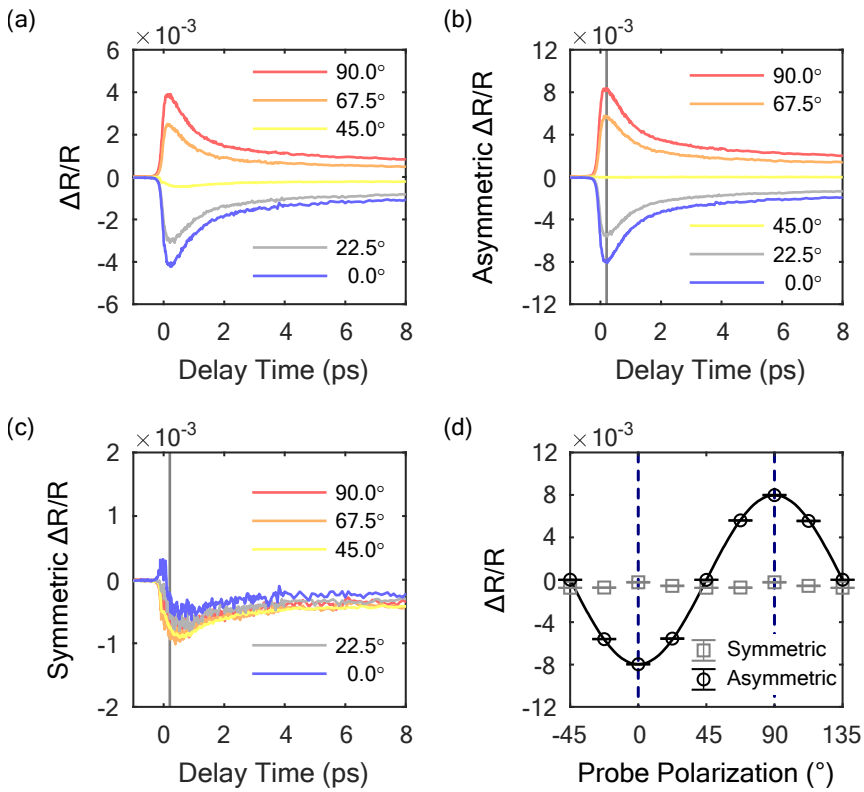

Figure 3.1: (a) Probe polarization dependent evolution of the photo-reflectivity of $Ba(Fe_{0.955}Co_{0.045})_2As_2$ single crystal measured as functions of pump-probe delay time τ_d at 30 K below T_{SDW} and T_S. Fluences are set to 120 μJ/cm^2 for pump incidence and 20 μJ/cm^2 for probe incidence. Labels mean angle between the probe polarization and the crystal orientation $[110]_{\mathrm{tetr}}$. (b) Asymmetric photo-reflectivity is obtained by Eq. (3.2a) and (c) symmetric photo-reflectivity is obtained by Eq. (3.3a) respectively. (d) Peak values of the asymmetric (circle) and the symmetric (square) photo-reflectivities are measured at $\tau_d = 0.2$ ps as functions of θ. A solid guide line is a simple sinusoidal function of $\Delta R/R \propto \sin(2\theta)$ where θ is the probe polarization. Dashed lines indicate the crystal orientation of $[110]_{\mathrm{tetr}}$, parallel to Fe-Fe bonding.

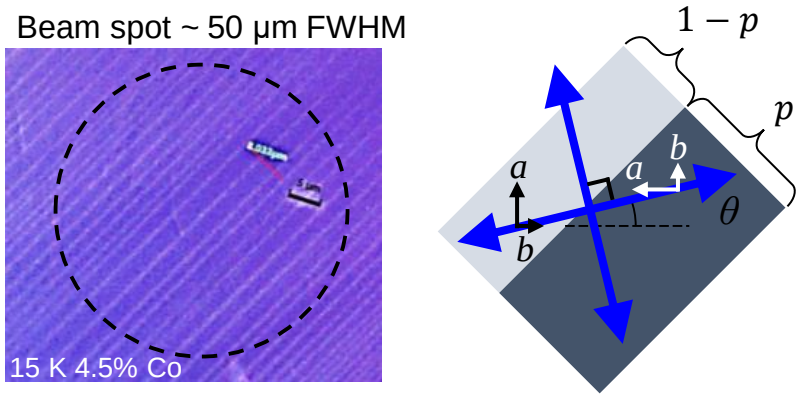

Figure 3.2: Polarized optical microscope image measured at 30 K, and schematic diagram of the photo-reflectivity measured at the twin-domain region.

where θ is orientation of the linear probe polarization from the crystallographic axis of $[110]_{\mathrm{tetr}}$. ΔR_a and ΔR_b are the photo-reflectivity when θ is parallel to the Fe-Fe bonding directions of $[100]_{\mathrm{orth}}$ or $[010]_{\mathrm{orth}}$. p is an area ratio of twin-domain within measuring spot. If $p = 0.5$, the measured photo-reflectivity does not show any dependence on θ. As displayed in Fig. 2.1(a), the value of p gradually varies depending on the probing spot, resulting in the spatial variation of the photo-reflectivity.

The photo-reflectivity is split into an asymmetric component ΔR_{asy} which depends on the probe polarization and a symmetric component ΔR_{sym} which

does not depend on the probe polarization:

$$\Delta R_{\text{asy}} \overset{\text{def}}{=} \Delta R(\theta) - \Delta R(\theta + 90^\circ) \tag{3.2a}$$

$$= (2p-1)(\Delta R_a - \Delta R_b)\cos 2\theta \tag{3.2b}$$

$$= (2p-1)(\Delta R_a - \Delta R_b) \quad \text{when } \theta = 0^\circ, \tag{3.2c}$$

$$\Delta R_{\text{sym}} \overset{\text{def}}{=} \Delta R(\theta) + \Delta R(\theta + 90^\circ) \tag{3.3a}$$

$$= \Delta R_a + \Delta R_b. \tag{3.3b}$$

Figure 3.1(b) displays probe polarization dependent evolution of the asymmetric photo-reflectivity, which clearly exhibits broken C_4 symmetry due to the electronic nematicity. The peak value measured at $\tau_d = 0.2$ ps as a function of the probe polarization in Fig. 3.1(d) is well fitted to a sinusoidal function of $\cos 2\theta$ as predicted by Eq. 3.2b. This suggest that the asymmetric photo-reflectivity originates from the electronic nematicity. We note that the value of asymmetric photo-reflectivity gradually varies depending on the measuring spot at the sample surface, but the symmetric photo-reflectivity does not as predicted by Eq. (3.2c) and Eq. (3.3b).

3.2.2 Asymmetric photo-reflectivity due to the B_{2g} nematicity

Figure 3.3 displays the asymmetric (left panel) and symmetric (right panel) photo-reflectivities as functions of pump-probe delay time and temperature measured at $Ba(Fe_{1-x}Co_x)_2As_2$ single crystals of x = 0–8.0 %. In all the

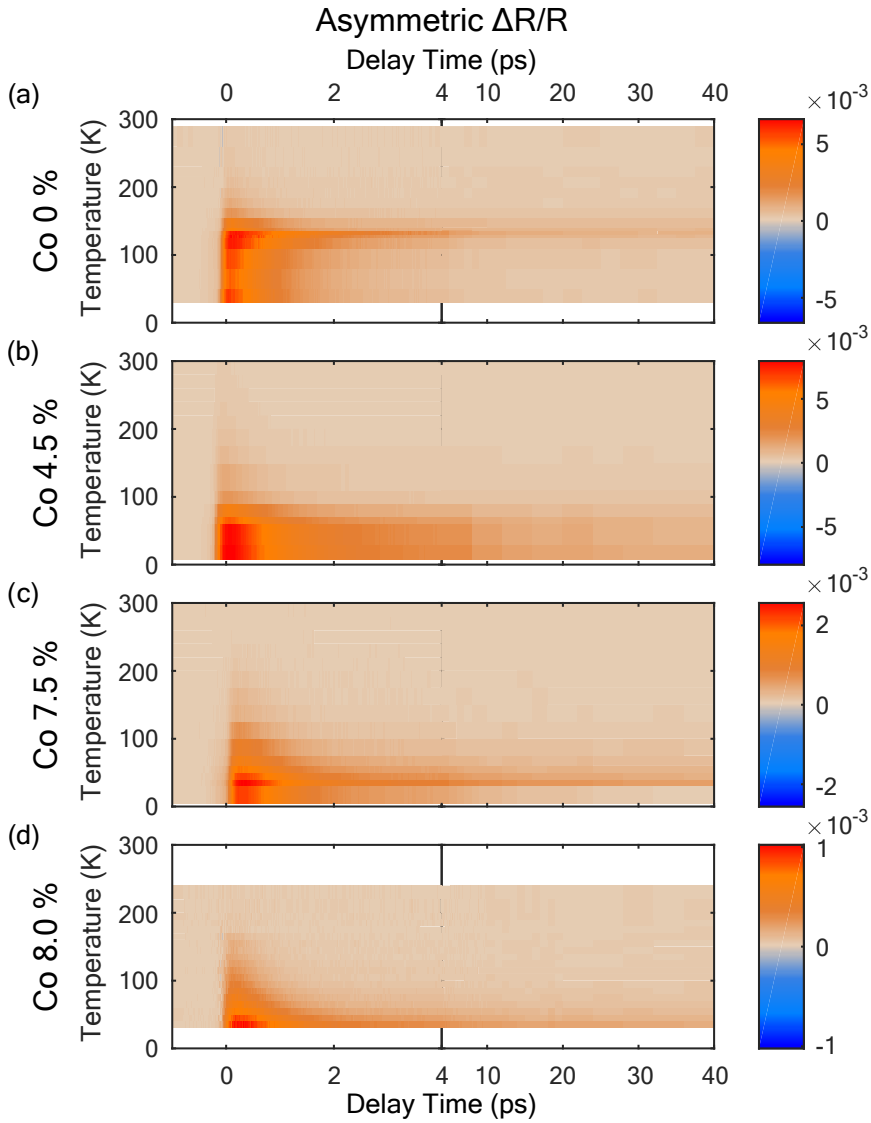

Figure 3.3: Asymmetric photo-reflectivity as functions of delay-time and temperature measured at $Ba(Fe_{1-x}Co_x)_2As_2$ of $x = 0$ %, 4.5 %, 7.5 %, and 8.0 %. Pump fluences are set to 63 μJ/cm^2 for $x = 0$ % in (a), 58 μJ/cm^2 for $x = 4.5$ % in (b), 51 μJ/cm^2 for $x = 7.5$ % in (c), and 52 μJ/cm^2 for $x = 8.0$ % in (d) respectively.

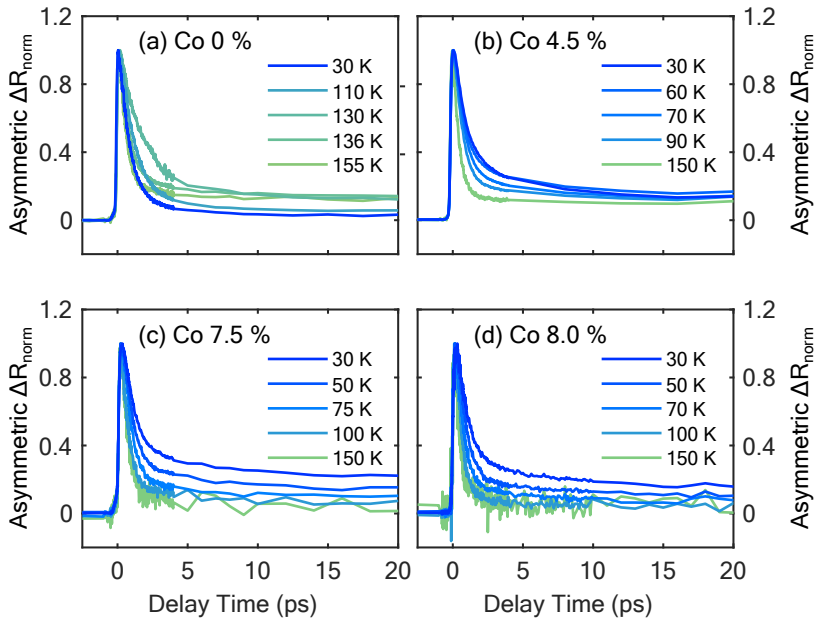

Figure 3.4: Selected temperature dependent evolutions of the asymmetric photo-reflectivity measured as functions of pump-probe delay time at (a) $x = 0$ %, (b) $x = 4.5$ %, (c) $x = 7.5$ %, and (d) $x = 8.0$ %. All data are normalized by initial peak values at each temperature and at each doping ratio x.

samples, the asymmetric photo-reflectivity has a considerable value far above T_S in under-doped side and above T_C in the over-doped side. This implies the presence of strong fluctuation of the B_{2g} nematicity without orthorhombic lattice distortion.

In all the samples, the asymmetric photo-reflectivity is recovered by a fast relaxation component of a picosecond (ps) timescale and following a slow component of a ten ps timescale. Figure 3.4 displays temperature dependent evolutions of the normalized asymmetric photo-reflectivity. Both the fast and slow components survive far above T_S without the orthorhombic lattice distor-

tion. The fast relaxation component survives up to much higher temperature and with much larger amplitude than the slow component.

Fit analysis is performed on the asymmetric photo-reflectivity using double exponential decay model of

$$\frac{\Delta R_{asy}(\tau_d)}{R} = A_0 + A_1 \exp\left(-\tau_d/\tau_1\right) + A_2 \exp\left(-\tau_d/\tau_2\right), \tag{3.4}$$

where A_0 is a constant background, A_1 is an amplitude of the fast component, A_2 is an amplitude of the slow component, τ_1 is a relaxation time of the fast component, and τ_2 is a relaxation time of the slow component.

Figure 3.5 displays the obtained fit parameters as functions of temperature. Temperature dependent evolutions of A_0, A_1, and A_2 exhibit the Curie-Weiss like behavior above the ordering temperatures of T_S in $x = 0$ % and 4.5 %, and T_C in $x = 7.5$ % and 8.0 %. Note that the values of A_1 is larger than the values of A_2 roughly by one order. A_2 is nearly fully reduced at 150 K for $x = 4.5$–7.5 %, but the fast component of A_1 survives up to higher temperature than 150 K. The observations consistently suggest that the nematic fluctuation has two distinctive origins.

3.2.3 Fit analysis on symmetric photo-reflectivity

The symmetric photo-reflectivities measured above T_S share common features of a sub-ps relaxation component of $\tau_e \sim 0.4$ ps followed by a coherent acoustic wave oscillation as displayed in Fig. 3.6.

The symmetric photo-reflectivity is fitted to a decay model of a single

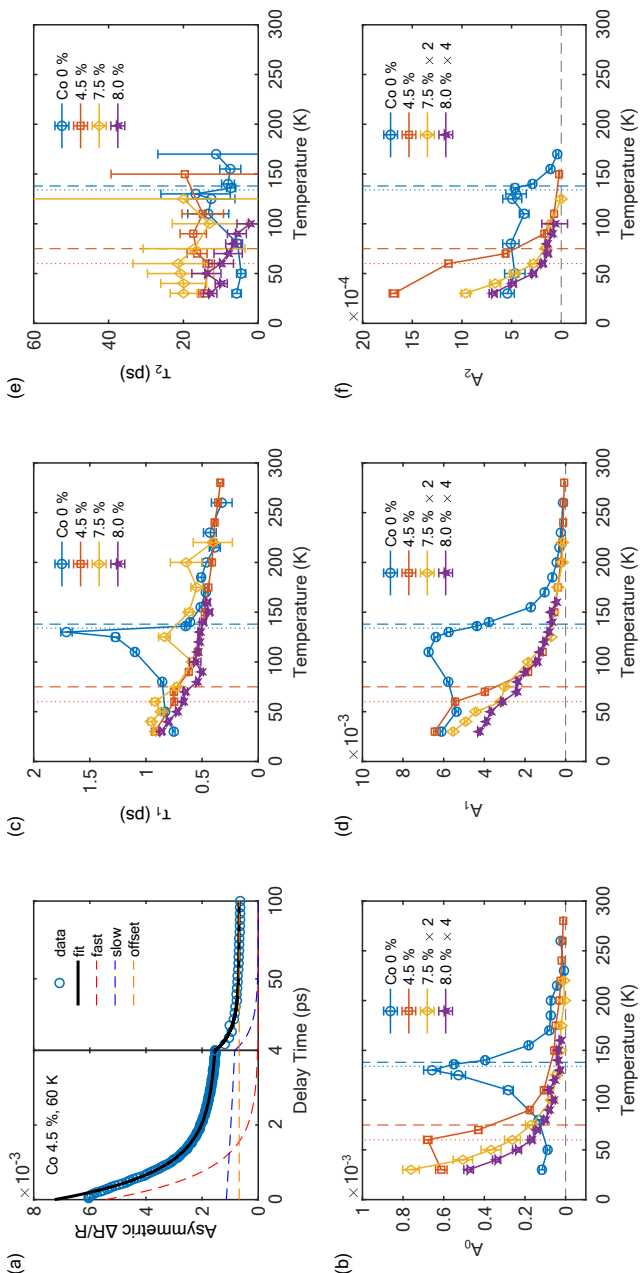

Figure 3.5: (a) Representative fitting curve using double exponential decay model of Eq. (3.4) and the corresponding experimental data of the asymmetric photo-reflectivity. Fit parameters of (b) constant background, (c)–(d) the fast component, and (e)–(f) the slow component are obtained as functions of temperature. For clarity, amplitudes of A_0, A_1, and A_2 are multiplied by factor two for $x = 7.5$ % and by factor four for $x = 8.0$ % respectively.

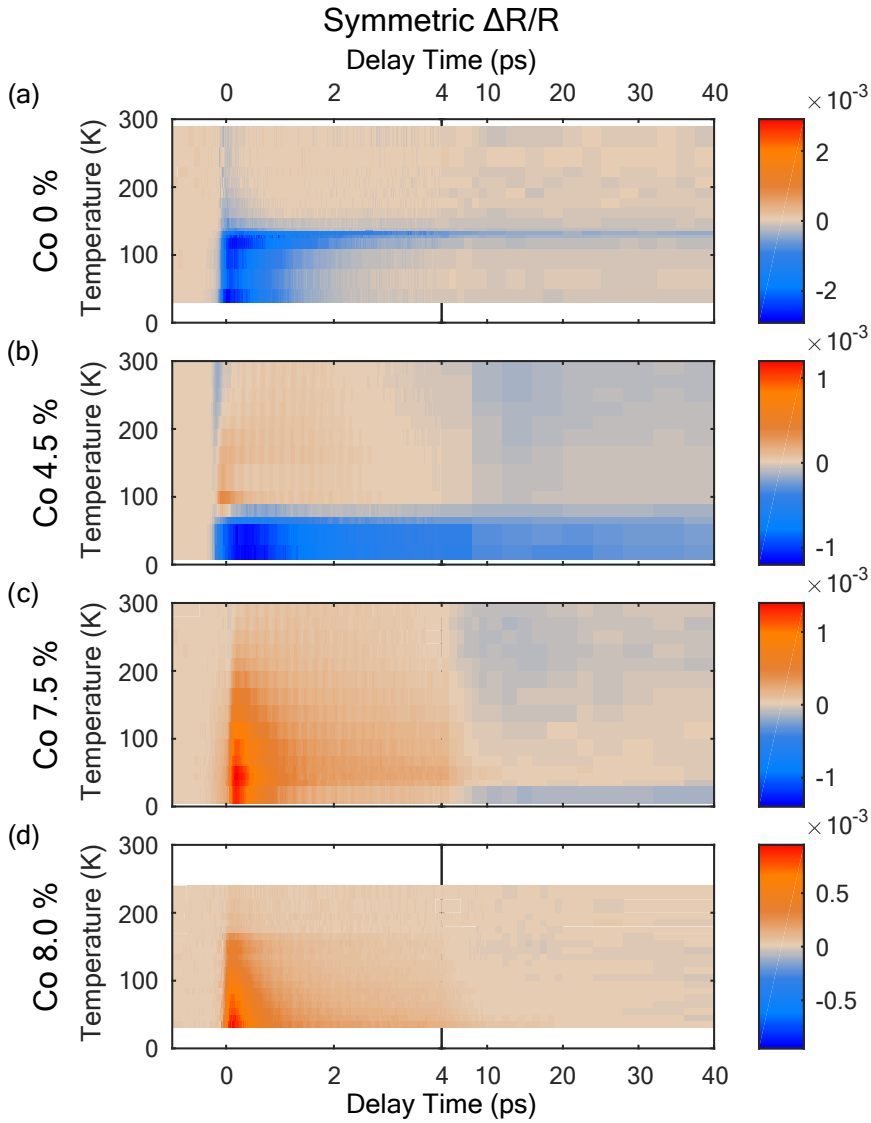

Figure 3.6: Symmetric photo-reflectivity as functions of delay-time and temperature measured at $Ba(Fe_{1-x}Co_x)_2As_2$ of $x = 0$ %, 4.5 %, 7.5 %, and 8.0 %. Pump fluences are set to 63 μJ/cm^2 for $x = 0$ % in (a), 58 μJ/cm^2 for $x = 4.5$ % in (b), 51 μJ/cm^2 for $x = 7.5$ % in (c), and 52 μJ/cm^2 for $x = 8.0$ % in (d) respectively.

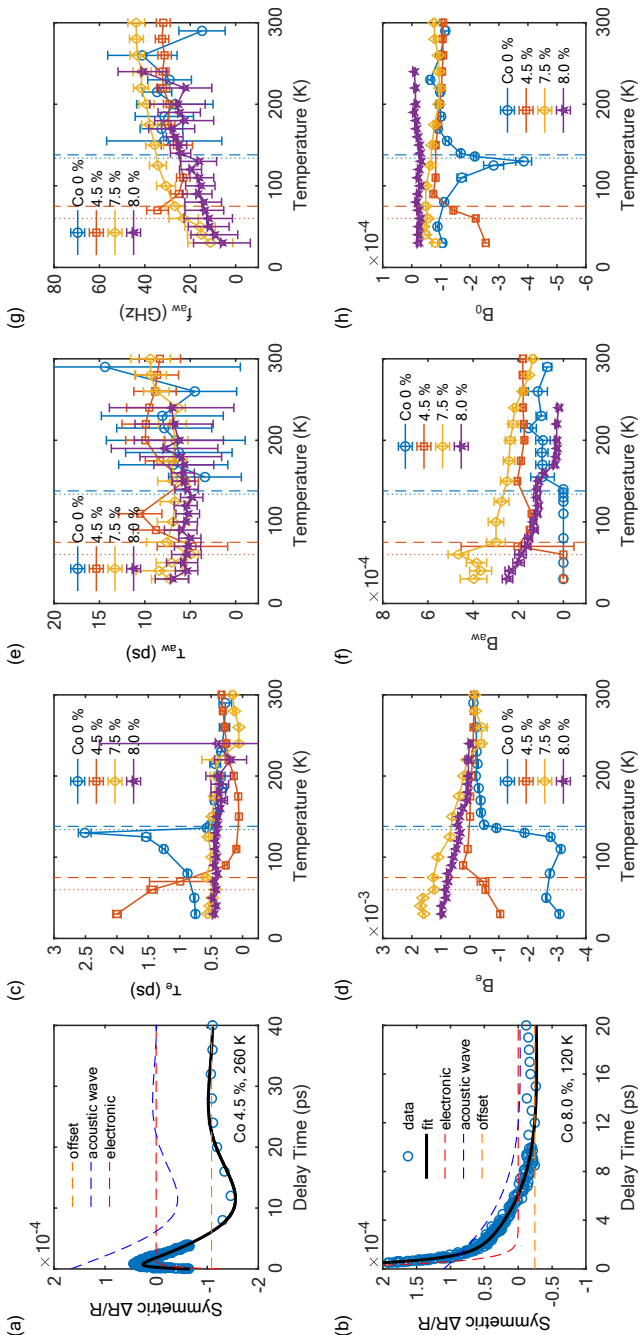

Figure 3.7: (a)–(b) Representative fitting to experimental data of the symmetric photo-reflectivity using Eq. (3.5). Obtained fit parameters (c)–(d) for electronic relaxation, (e)–(g) for acoustic wave oscillation, and (h) for constant background as functions of temperature.

exponential relaxation and an exponentially decaying sinusoidal function:

$$\frac{\Delta R_{sym}(\tau_d)}{R} = B_e + B_e \exp\left(-\tau_d/\tau_e\right) + B_{\mathrm{aw}} \exp\left(-\tau_d/\tau_{\mathrm{aw}}\right) \cos\left(2\pi f_{\mathrm{aw}} \tau_d + \phi_0\right), \tag{3.5}$$

where B_0 is a constant background, B_e and τ_e are an amplitude and a relaxation time of the electronic relaxation component. B_{aw} and τ_{aw} are an amplitude and a dephasing time of the coherent acoustic wave oscillation. f_{aw} and ϕ_0 are oscillation frequency due to the acoustic wave propagation along the depth from the surface. ϕ_0 is fixed to constant values. Doping dependent evolution of the fit parameters are displayed as functions of temperature in Fig. 3.7.

3.2.4 Quasiparticle dynamics across SDW gap and observations of coherent acoustic wave oscillations

Great coincidence of temperature dependent evolutions of τ_1 over $x = 0$–8.0 % suggest a particular origin for the fast relaxation process. Note that τ_1 of $x = 0$ % diverges as temperature approaches to $T_{\mathrm{SDW}} = 137$ K. Figure 3.8 displays the temperature dependent evolutions of τ_1, A_1, τ_e, and B_e of the undoped sample, exhibiting anomalous temperature trends near T_{SDW}. Their temperature dependent evolutions below T_{SDW} are well explained by the quasi-particle dynamics model [Kabanov et al., 1999]:

$$A \propto \frac{\left(\Delta\left(T\right) + k_B T/2\right)^{-1}}{1 + \gamma\sqrt{\frac{2k_B T}{\pi\Delta(T)}} \exp\left[-\Delta\left(T\right)/k_B T\right]}, \tag{3.6}$$

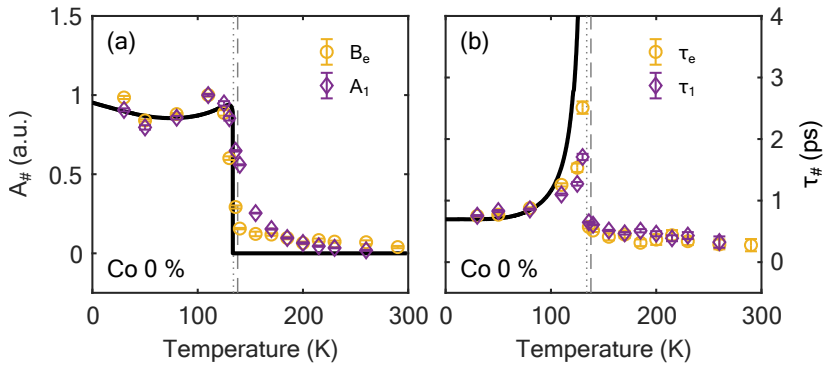

Figure 3.8: (a) Amplitudes of the fast asymmetric relaxation component A_1 and of the sub-ps symmetric relaxation component B_e. (b) Relaxation time of the fast asymmetric relaxation component τ_1 and of the sub-ps symmetric relaxation component τ_e. Asymmetric fit parameters of A_1 and τ_1 are obtained by fit analysis using Eq. (3.4). Symmetric fit parameters of B_e and τ_e are obtained by fit analysis using Eq. (3.5). Solid guide lines are generated by using Eq. (6) for amplitudes and Eq. (28) for relaxation times in Ref. [Kabanov et al., 1999] as described in main text.

$$\tau \propto \frac{\ln\left(F + \exp\left[-\Delta\left(T\right)/k_B T\right]\right)}{\Delta\left(T\right)^2}, \tag{3.7}$$

where constant values of $\gamma = 1.3$ and $F = 0.07$ are obtained by hand to match the fit curves to the data. $\Delta\left(T\right)$ employ BCS-like temperature dependent isotropic gap of $\Delta(0) = 21$ meV reported by the optical spectroscopy study [Nakajima et al., 2012]. The presence of the SDW order highly affects to the ps relaxation dynamics in both of the asymmetric and the symmetric photo-reflectivities. The phonon-bottleneck effect state that the quasiparticle dynamics across small charge gap slows down because the recombination process becomes hard to occurs. The observed temperature dependent evolutions in both of the asymmetric and symmetry photo-reflectivity relaxation below T_{SDW} consistently suggest the development of the isotropic SDW gap.

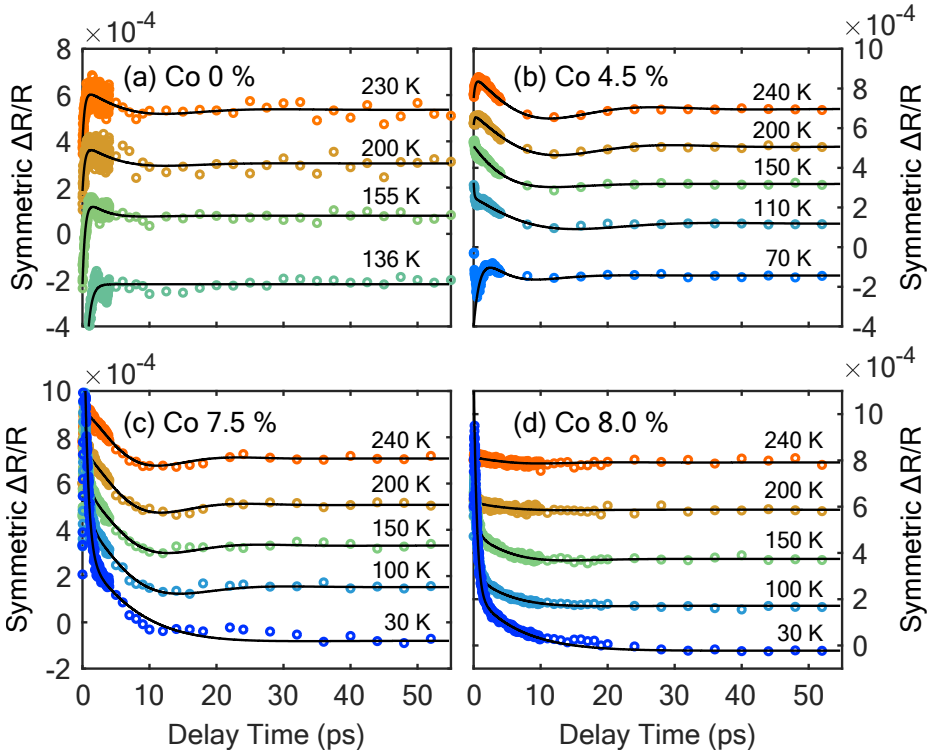

Figure 3.9: Temperature dependent evolutions of the coherent acoustic wave oscillation in the symmetric photo-reflectivity. Experimental data (open circles) are well fitted to solid fitting lines of Eq. (3.5). For clarity, each data is shifted by an interval of 2×10^{-4}.

The absence of slowing down behavior at under-doped sample is well corroborated by doping-induced gap broadening effect [Nakajima et al., 2012]. Therefore, we carefully speculate that the fast component is the spin-related nematic fluctuation and, therefore, the slow component is the lattice-related nematic fluctuation. The interpretation is corroborated by a previous ultrafast polarimetry investigation on the static nematic order in under-doped $Ba(Fe_{1-x}Co_x)_2As_2$ [Patz et al., 2014].

Finally, we note that assigning the slow component to the lattice-nematic fluctuation is also consistent to our observation of coherent acoustic wave oscillations in the symmetric photo-reflectivity. Figure 3.9 displays the symmetric photo-reflectivity measured at selected temperatures demonstrating the existence of the coherent acoustic wave oscillations over $x = 0$–8.0 %. The acoustic wave oscillations of the photo-reflectivity accompany the phonon-phonon scattering process [Thomsen et al., 1986]. Therefore, its dephasing timescale comparable to the slow component of the symmetric photo-reflectivity implies the relevance to the lattice degrees of freedom.

3.3 Conclusion

In conclusion, near-infrared pump-probe experiments is performed at the electron-doped $Ba(Fe_{1-x}Co_x)_2As_2$ single crystals with $x = 0$ %, 4.5 %, 7.5 %, and 8.0 %. The measured photo-reflectivity are consisting of symmetric response independent on the probe polarization and asymmetric response dependent on the probe polarization. Temperature-dependent evolutions of the asymmetric photo-reflectivity show that nematic fluctuation strongly present near over wide range of doping even at the tetragonal phase, where the lattice C_4 symmetry is preserved. Our observations of quasiparticle dynamics across T_{SDW} and the coherent acoustic wave oscillations suggest that the asymmetric photo-reflectivity successfully features both of the spin- and lattice-nematic fluctuations having the distinctive timescales respectively.

4. Measurement of small reflectivity anisotropy in the nematic state and its non-equilibrium dynamics

Spectroscopic investigations of a small nematic anisotropy requires a challenging signal-to-noise ratio. Photo-elastic modulator (PEM) with a lock-in technique make polarimetry experiments get notably high signal-to-noise ratio [Weightman et al., 2005,Tros and Woutersen, 2015,Oppermann et al., 2019]. However, measuring an equilibrium optical anisotropy of the single crystalline sample is obscured by a geometric anisotropy, differentiating reflection coefficients for s- and p-polarized lights. Fresnel equations state that even optically isotropic materials could have the considerable geometric anisotropy due to a non-zero angle of incidence. In the transmission measurements, the perfect normal incidence is easily achievable for the transparent materials. However, it is not feasible in the reflection measurement, inevitable for non-transparent materials.

In this chapter, I present a new experimental method to investigate the reflectivity anisotropy due to the nematicity. As a demonstration, I display the experimental result on $Ba(Fe_{0.955}Co_{0.045})_2As_2$ single crystal. Numerical simulations demonstrate that our method is highly reliable in conventional experimental condition. At the end of this chapter, our method is used to perform the time-resolved experiment and confirms that ultrafast photo-excitation suppresses the reflectivity anisotropy originating from the nematic order.

4.1 Introduction

Optical anisotropy appears in various materials bearing lattice, electronic, or magnetic anisotropies. Birefringent materials of large optical anisotropy have been extensively investigated and employed in various optical techniques such as second-harmonic-generations, photo-elastic modulations, and liquid-crystal displays. Even small anisotropy can often play an important role for other physical properties of interest [Tros and Woutersen, 2015, Oppermann et al., 2019, Weightman et al., 2005].

Recently electronic nematicity, breaking rotational symmetry of lattice, has attracted a great deal of attention with regard to the relation with high-T_C superconductivity. The nematic phase precedes the superconductivity in numerous correlated electronic systems such as iron-pnictide [Kuo et al., 2016], cuprate [Daou et al., 2010,Sato et al., 2017], heavy Fermion materials [Okazaki et al., 2011, Riggs et al., 2015], and topological superconductors [Sun et al., 2019]. In Fe-based superconductors, the nematic order in under-doped materials is accompanied with a structural phase transition and exhibits clear electronic anisotropy as confirmed in various experiments such as strain-dependent transport measurement [Kuo et al., 2016], angle-resolved photo-emission spectroscopy [Yi et al., 2011], and optical spectroscopy [Nakajima et al., 2012]. In optimal- and over-doped materials, the structure transition is fully suppressed. However, the electronic anisotropy still remains strongly fluctuating

and a nematic quantum critical point is supposed to exist near the optimal doping, suggesting that the nematic fluctuations may play an important role for the superconductivity [Kuo et al., 2016]. As doping further increases, a new type of nematic order appears in heavily hole-doped materials. That is, the orientation of electronic nematicity is rotated by 45 degrees without any signature of corresponding lattice symmetry breaking. It has been suggested that the change of the nematic orientation is accompanied with crossover of the superconducting gap symmetry from a nodeless one to a nodal one [Liu et al., 2019, Ishida et al., 2019]. Therefore, investigation of even small electronic nematicity is important to understand the nematic fluctuations and the superconductivity in Fe-based materials.

Study on a small nematic response requires a challenging signal-to-noise ratio for spectroscopic investigations such as angle-resolved photo-emission spectroscopy. Optical polarimetry experiments using photo-elastic modulator (PEM) with a lock-in technique provide notably high signal-to-noise ratio [Weightman et al., 2005,Tros and Woutersen, 2015,Oppermann et al., 2019]. However, measurement of a small optical anisotropy is usually obscured by a geometric anisotropy, which differentiates reflection or transmission coefficients for s- and p-polarized electromagnetic waves. Fresnel equations state that the geometric anisotropy could be considerable at a non-zero angle of incidence even in optically isotropic materials. For transparent materials, the transmission measurements at the perfect normal incidence can be free from the geometric effect. However, the normal incidence to avoid the geometric anisotropy

is not feasible for the reflection measurement, inevitable for non-transparent materials. As a result, spectroscopic investigations of the anisotropy of non-transparent materials have been limited or requires only specific experimental conditions such as precise sample-rotation alignments [Weightman et al., 2005].

In following sections, I will show a new experimental method to investigate the reflectivity anisotropy and its non-equilibrium dynamics. Our method does not require any specific experimental conditions such as precise alignment of the sample rotation angle and the principal axes of the anisotropy are easily characterized. This makes our method appropriate for studying electronic nematicity and its fluctuations in correlated electron systems such as cuprate, pnictide, and heavy Fermion superconductors.

4.2 Details of experimental setup

For polarimetry experiment, a PEM is employed to sinusoidally modulates the phase retardation of the probe beam at a frequency $\omega = 47$ kHz. The reflectivity anisotropy due to the modulation of the probe polarization is obtained as a 2ω signal through the first lock-in amplifier. In the time-resolved experiment, the pump beam is modulated by an optical chopper and transient change in the reflectivity anisotropy is measured through the second lock-in amplifier. Schematic diagram of the experimental setup is displayed in Fig. 4.1. Note that our optical setup is basically same as the one by [Tros and Woutersen, 2015] except that the reflectivity anisotropy is measured at a crystalline sample, not

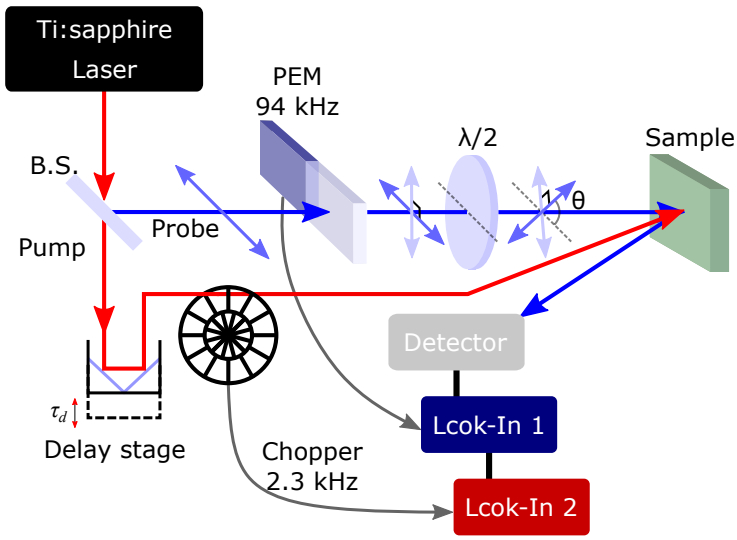

Figure 4.1: Schematic diagram of the experimental setup. Ultrafast pulse is split into pump and probe beams after a beam splitter (B.S.). Optic axis of PEM is set to be 45° with respect to the incoming probe polarization. After the PEM, the probe polarization is varied by rotating half wave-plate.

the transmittance of a liquid sample.

The Jones calculus on our experiment shows that the 2ω lock-in signal $R_{2\omega}$ is a sinusoidal function of the angle between the probe polarization and the orientation of the crystal anisotropy as follows:

$$\begin{aligned} R_{2\omega}(\alpha,\theta,\phi) =& J_2(A)[(|r_{aa}|^2 - |r_{bb}|^2 - |r_{ab}|^2 + |r_{ba}|^2)\cos(2\theta - 2\phi) \\ & - 2\Re(r_{aa}^* r_{ab} + r_{ba}^* r_{bb})\sin(2\theta - 2\phi)], \end{aligned} \tag{4.1}$$

where α is the angle of incidence, θ is the orientation of the probe polarization incident to the sample, and ϕ is the orientation of a crystal axis as shown in

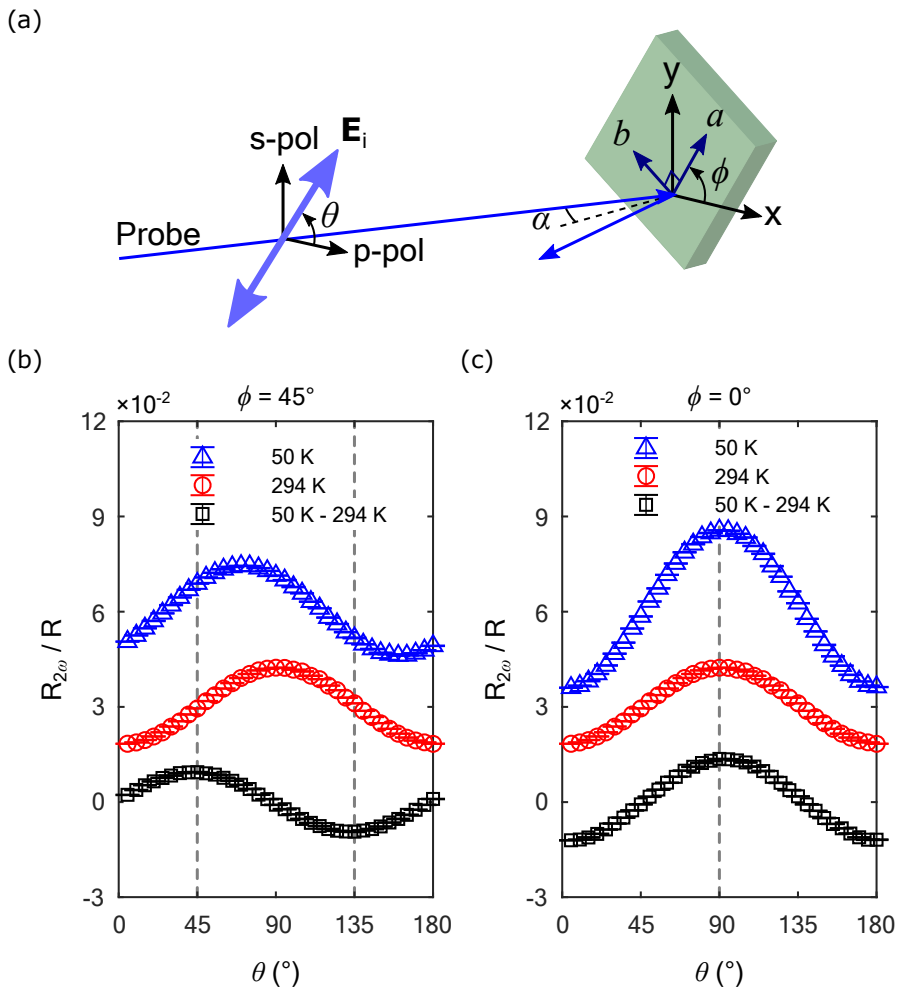

Figure 4.2: Experimental geometry of the sample and the probe polarization, and experimental results on $Ba(Fe_{0.955}Co_{0.045})_2As_2$ single crystals. (a) The orientations of the probe polarization θ and of the crystal axis ϕ are shown with respect to the plane of incidence. In the experiment, the angle of incidence α is 10°. The 2ω lock-in signal $R_{2\omega}/R$ is shown for the cases of (b) $\phi = 45°$ and (c) $\phi = 0°$. Data measured in the nematic state at 50 K (blue open triangles) and in the normal state at 294 K (red open circles) are vertically shifted for clarity. Black open squares are obtained by subtracting data at 294 K from data at 50 K.

Fig. 4.2(a). $J_2(A)$ is a Bassel function of the first kind and A is the modulated phase angle by PEM. The values of θ and ϕ are indicated with respect to the plane of incidence at the sample surface. r_{ij} is the complex reflectivity coefficient of the sample where i and j indicate polarizations of the incident and the reflected electric fields, respectively. For example, r_{ab} indicate the complex reflectivity coefficient when the incident polarization is parallel to the crystal axis a and the reflected polarization is parallel to the crystal axis b. Note that r_{ij} is a function of α and ϕ, but does not depend on θ. If α is small enough to be considered as a normal incidence case, $|r_{ab}|$ and $|r_{ba}|$ are negligibly small compared to $|r_{aa}|$ and $|r_{bb}|$ [Graham and Lee, 2011], and Eq. (4.1) can be approximated to

$$\frac{R_{2\omega}(\alpha \approx 0, \theta, \phi)}{R} \approx 2J_2(A)\frac{|r_{aa}|^2 - |r_{bb}|^2}{|r_{aa}|^2 + |r_{bb}|^2}\cos(2\theta - 2\phi)\,. \tag{4.2}$$

In case of half-wave modulation, $A = \pi$ and $2J_2(\pi) = 0.9708$.

4.3 Results and discussions

4.3.1 Experimental demonstration of the reflectivity anisotropy in the nematic state

Figure 4.2 displays experimental data of $R_{2\omega}/R$ measured on $Ba(Fe_{0.955}Co_{0.045})_2As_2$ single crystals. In the nematic state, the crystal has orthorhombic lattice, whose principal axes of $[100]_{\mathrm{orth}}$ and $[010]_{\mathrm{orth}}$ are parallel to the Fe-Fe bonding directions. Two pieces of samples are prepared on a Cu-plate with different crystal orientations of $\phi = 45°$ and $0°$. In the normal state at 294 K, $R_{2\omega}/R$

(open circles) exhibits the same sinusoidal dependence in both cases of $\phi = 45°$ in Fig. 4.2(b) and $\phi = 0°$ in Fig. 4.2(c). We note that this polarization dependence in the sample without nematic anisotropy originates from the geometric effect in the measurement at non-zero angle of incidence. In the nematic state at 50 K, on the other hand, $R_{2\omega}/R$ (open triangles) features a phase-shift from the normal state response for $\phi = 45°$ in Fig. 4.2(b) while the amplitude is enhanced without a phase-shift for $\phi = 0°$ in Fig. 4.2(c). This implies that different functions of θ and ϕ due to the nematic order is added up to the normal state signal. These data show that the geometric anisotropy due to the non-zero angle of incidence has a comparable amplitude to the nematic anisotropy.

To remove the geometric anisotropy, we subtract the normal state signal at 294 K (open circles) from the reflectivity anisotropy at 50 K (open triangles):

$$\frac{\delta R_{2\omega}}{R} = \left.\frac{R_{2\omega}(\alpha,\theta,\phi)}{R}\right|_{T<T_{\mathrm{nem}}} - \left.\frac{R_{2\omega}(\alpha,\theta,\phi)}{R}\right|_{294\mathrm{K}}. \tag{4.3}$$

Obtained nematic anisotropies (open squares) clearly features a cosine function of $(2\theta - 2\phi)$, as displayed in Fig. 4.2(b) for $\phi = 45°$ and Fig. 4.2(c) for $\phi = 0°$, which agrees with Eq. (4.2).

4.3.2 Numerical simulation on the reflectivity anisotropy in the nematic state

Numerical simulation of the reflectivity anisotropy confirms that the experimental approach according to Eq. (4.3) can successfully represent the nematic anisotropy as displayed in Fig. 4.3(a). For the simulation on the normal

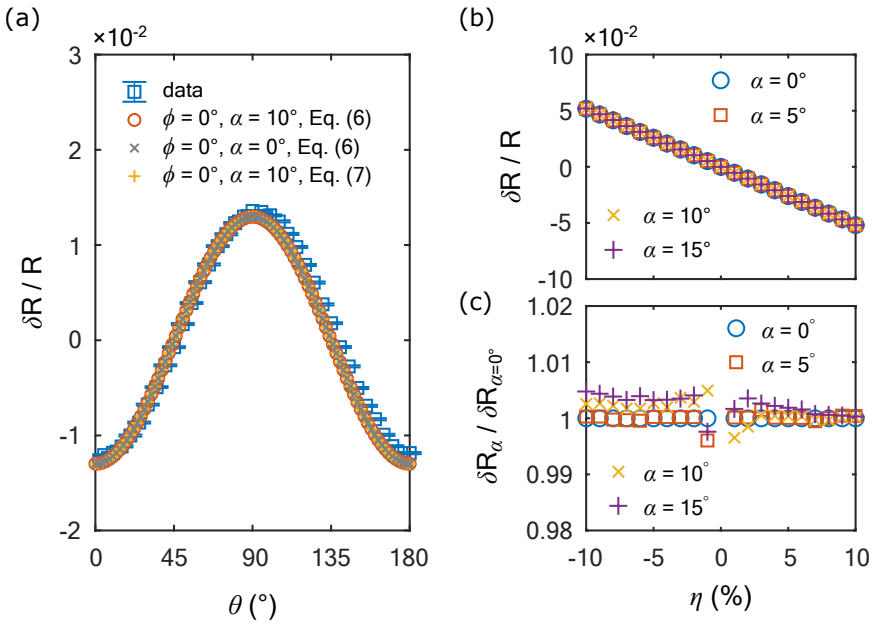

Figure 4.3: Simulations of the reflectivity anisotropy. (a) Comparison of the experimentally obtained nematic anisotropy (open square) with simulated ones for $\alpha = 10°$ and $\phi = 0°$ by Eq. (4.6) and Eq. (4.7). All of them agree with the the exact case of $\alpha = 0°$ at $\phi = 0°$ (symbol $\times$). (b) Nematic anisotropy simulated for various values of α by Eq. (4.6). (c) The simulated nematic anisotropy is normalized by the normal incidence case. η is a relative ratio of a half of birefringence $\delta n/2$ to the refractive index of the isotropic case n_{ab}. Refractive index n_a and n_b for the nematic state is varied as described in the text.

state, we employed a virtual refractive index of $n_{ab} = 2.865 + 2.53i$, and $n_c = 1.62 + 2.05i$ at the photon energy of 1.55 eV. The value of n_{ab} is from the experimental results on $BaFe_2As_2$ single crystal measured at room temperature by spectroscopic Ellipsometer, and the value of n_c is extracted from published data [Moon et al., 2013]. For the nematic state, we increased (decreased) the real part and decreased (increased) the imaginary part of n_a (n_b)

by a relative ratio η such that $\delta n = n_a - n_b \propto 2\eta \times n^*_{ab}$, which is consistent to the change observed in the nematic state [Moon et al., 2013]. Reflectivity of s-polarization R_s and p-polarization R_p for $\phi = 0^\circ$ were calculated using WVASE (Woollam Co.). Reflectivity and its anisotropy at arbitrary polarization were calculated as below:

$$R(\alpha, \theta) = R_p(\alpha) \cos^2 \theta + R_s(\alpha) \sin^2 \theta, \tag{4.4}$$

$$\frac{R_{\rm sim}(\alpha, \theta)}{R} = \frac{R(\alpha, \theta) - R(\alpha, \theta + 90^\circ)}{R(\alpha, \theta) + R(\alpha, \theta + 90^\circ)}, \tag{4.5}$$

$$\frac{\delta R_{\rm sim}}{R} = \frac{R_{\rm sim}(\alpha, \theta)}{R}\bigg|_{n_a \neq n_b} - \frac{R_{\rm sim}(\alpha, \theta)}{R}\bigg|_{n_a = n_b}. \tag{4.6}$$

As displayed in Fig. 4.3(a), our experimental result (open square) of $\phi = 0^\circ$ by Eq. (4.3) is well reproduced by the numerical simulation (open circle) of Eq. (4.6) with $\eta = 5$ % variation of the refractive index for the nematic state. Furthermore, they match well with the true reflectivity anisotropy of the material for the case of the normal incidence (symbol $\times$), where the geometric anisotropy is absent.

To demonstrate the reliability of Eq. (4.3), we performed the simulation for $\alpha \leq 15^\circ$ and for η up to $\pm 10\%$. As displayed in Fig. 4.3(b), $\delta R_{\rm sim}/R$ is proportional to η. The angle of incidence α does not affect the result within the order of 10^{-4} of the absolute reflectivity anisotropy ratio as displayed in Figs. 4.3(b) and (c).

We note that our method can be extended to materials of small nematicity even when the high temperature isotropic phase is not accessible. In a nematic state, nematic twin domains are easily found in a single piece of a

sample. Because the geometric anisotropy is expected to be similar in the two twin domains, we can eliminate the geometric effect from the difference of the reflectivity measured on the two different domains. For the given case of the crystal orientation of ϕ, the twin domain should have $\phi' = \phi + 90°$. Therefore, the reflectivity anisotropy can be obtained as follows:

$$\frac{\delta R(\theta, \phi)}{R} = \frac{R_{2\omega}(\theta, \phi) - R_{2\omega}(\theta, \phi + 90°)}{2R}. \tag{4.7}$$

One can measure on the twin domains by simply translating the sample surface, which should be appropriate in most of samples in a nematic state. Such a measurement could be performed also on a single domain sample as well by rotating the sample if the crystal angle could be precisely controlled. Figure 4.3(a) shows that the result from this method also agrees nicely with the true reflectivity anisotropy for the normal incidence case.

4.3.3 Time-resolved experiment on the reflectivity anisotropy in the nematic state

Finally transient reflectivity anisotropy $\Delta(\delta R)/R$ of $Ba(Fe_{0.955}Co_{0.045})_2As_2$ single crystal is measured at 50 K upon pumping with 800 nm photons. Our results clearly show that the reflectivity anisotropy due to the nematic order is suppressed by ultrafast photo-excitation as displayed in Fig. 4.4(a). As discussed in Chapter 4, the nematic responses of Fe-based superconductors have been observed in pump-probe experiments even in the tetragonal structure. However, because the pumping with linearly polarized photons inherently

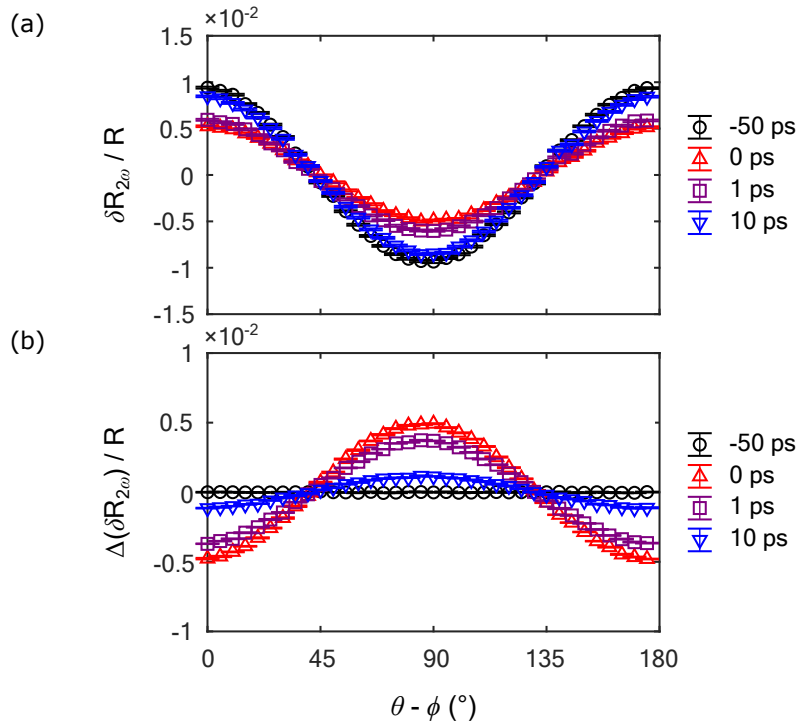

Figure 4.4: Pump-probe results of the reflectivity anisotropy. (a) Nematic anisotropy $\delta R/R$ of $Ba(Fe_{0.955}Co_{0.045})_2As_2$ single crystal at 50 K obtained by Eq. (4.3) and (b) its transient change $\Delta(\delta R)/R$ measured at various delay times τ_d. The pump fluence is fixed at 31 $\mu J/cm^2$.

possesses an anisotropic nature, the observed nematicity in the pump-probe experiment can be questioned whether it is the intrinsic nematicity. We found that the change of the reflectivity anisotropy upon pumping does not depend on the polarization of the pump pulses. Our simultaneous observation of $\delta R/R$ and $\Delta(\delta R)/R$ demonstrates that the nematic order is suppressed by the photo-excitation without an pump-induced anisotropy and, therefore, assures that previous time-resolved studies on the nematicity indeed reflects the intrinsic

nematic properties of the iron pnictides [Patz et al., 2014, Shimojima et al., 2019].

4.4 Conclusion

In summary, we present experimental method to study the optical anisotropy by reflection experiment. As a demonstration, we measure the nematic anisotropy of $Ba(Fe_{0.955}Co_{0.045})_2As_2$ single crystal. Numerical simulations confirm that the experimentally observed data are highly reliable. Successive time-resolved experiment on the nematic anisotropy assures that the ultrafast photo-excitation simply suppresses the nematic anisotropy of the iron pnictides.

5. Strain-induced rotation of nematic reflectivity anisotropy in electron under-doped $Ba(Fe_{0.955}Co_{0.045})_2As_2$

In this chapter, I present strain-dependent investigation of time-resolved reflectometry on the electron-doped $Ba(Fe_{0.955}Co_{0.045})_2As_2$. As discussed in previous chapters, the sample shows a typical B_{2g} nematicity of the iron pnictides with an antiferromagnetic order in an orthorhombic crystal structure. However, the photo-reflectivity under uniaxial-strain along $[110]_{\mathrm{tetr}}$ reveals an unexpected nematicity of which C_4 symmetry breaking orientation is rotated. Successive reflectivity anisotropy measurements in the equilibrium state without photon pumping confirm that the peculiar rotation by about 20° is induced not by the photo-doping after pumping but by the uniaxial-strain. The details of the experimental results will be discussed.

5.1 Introduction

Electronic nematicity of broken C_4 symmetry has created enormous interest in relation to Fe-based superconductivity. Most of Fe-based materials share a common feature that the nodeless superconductivity emerges as the B_{2g} nematic order is suppressed by chemical doping or pressure [Paglione and Greene, 2010, Chubukov, 2012]. Extensive studies in the vicinity of the superconducting dome have suggested quantum criticality possibly of the electronic

nematicity that could provide the paring interaction for the high-T_C superconductivity [Shibauchi et al., 2014,Kuo et al., 2016,Liu et al., 2016]. Interestingly, recent studies on a heavily hole-doped system $RbFe_2As_2$ have discovered another nematic state of B_{1g} symmetry, whose principal axis of the nematicity is rotated by 45° from the B_{2g} nematic order [Liu et al., 2019,Ishida et al., 2019]. It has also been suggested that the change of the superconducting gap symmetry could be coupled to the symmetry of the nematic order [Liu et al., 2019]. Theoretical studies have suggested that the spin fluctuations play an important role in determining the nematic state of B_{2g} and B_{1g} symmetries [Onari and Kontani, 2019, Borisov et al., 2019].

Numerous investigations of the nematic phase have employed uniaxial strain to detwin single crystals. The single crystals of the orthorhombic lattice in the B_{2g} nematic state have stripe-type twin-domains. The small domain width of a few micrometers makes experimental investigations of the intrinsic nematic properties challenging. Most of experimental studies on the anisotropic electronic properties in the B_{2g} nematic state have been performed on the detwinned sample exhibiting a large enough single domain under the uniaxial strain [Tanatar et al., 2010, Chu et al., 2010, Yi et al., 2011, Kasahara et al., ,Nakajima et al., 2012,Kim et al., 2013,He et al., 2017,Pfau et al., 2019,Huh et al., 2019]. The strain-induced conjugate field of the nematic order parameter has been widely used to measure elastoresistivity tensor, expected to be proportional to the nematic susceptibility [Kuo et al., 2013, Shapiro et al., 2016, Kuo et al., 2016]. However, the first principle calculations show

that the Fermi-surface of the iron pnictide is easily modulated by the uniaxial strain [Tomić et al., 2012, Tomić et al., 2013]. Recent experimental studies have also revealed that uniaxial strain can be a tuning parameter for the superconductivity as well as the nematic and the long-range magnetic order in iron pnictide [Tam et al., 2017,Ikeda et al., 2018,Willa et al., 2019,Malinowski et al., 2019]. Therefore, the influence of the applied strain needs to be carefully considered.

Ultrafast pump-probe reflectometry provides a unique opportunity to investigate the nematicity of the Fe-based materials. Relatively small spot size and a great signal-to-noise ratio make it possible to measure the nematic response even on the twined crystals. Indeed, the photo-reflectivity measured on various Fe-based materials clearly features the broken four-fold symmetry due to the B_{2g} nematicity without any external pressure applied [Luo et al., 2017,Liu et al., 2018,Thewalt et al., 2018]. In addition, time-resolved polarimetry investigation has successfully distinguished nematic fluctuations of the structural and magnetic origins based on their distinct relaxation timescales [Patz et al., 2014]. Furthermore, extensive time-resolved studies have revealed the strong coupling between the lattice modulation and the electronic structure, which should affect the spin-density-wave, nematic, and superconducting orders. [Kim et al., 2012, Gerber et al., 2015, Gerber et al., 2017]

5.2 Results and discussions

5.2.1 Applying uniaxial-strain by affixing the sample to piezo-stack

To apply uniaxial tensile-strain, the sample is affixed with silver epoxy to a piezo-stacks (Part No: PSt 150/2×3/5 vacuum/cryo, Piezomechanik GmbH). The poled direction of the piezo-stack is aligned to be parallel to $[110]_{\mathrm{tetr}}$ as displayed in Fig. 5.1(d). Crystal orientations were identified before the attachment by Laue-XRD measurements. Surface of the sample is cleaved in the ambient condition and, then, immediately transferred to the cryostat.

As temperature cools down, the piezo-stacks lengthen along their poled direction while the sample contracts [da Luz et al., 2009]. Thermal expansion coefficient of piezo-stack is -5×10^{-6} K^{-1} along the poled direction at 293 K. Our sample has isotropic thermal expansion coefficient of 8×10^{-6} K^{-1} at 293 K. Therefore, tensile-strain is applied to the affixed sample along the crystal orientation aligned parallel to the poled direction. Note that the tensile-strain due to the differential thermal contractions is much larger than the achievable strain by applying DC voltage on the piezo-stack [Thewalt et al., 2018, da Luz et al., 2009, Kuo, 2014]. The maximum stroke of the piezo-stack is about 6.6 μm per 5 mm length at 293 K, and it decreases to 20 % at 77 K and to 5 % at 4 K.

5.2.2 Rotation of C_4 symmetry breaking under uniaxial-strain

Figure 5.1 displays the photo-reflectivity of the sample affixed on a copper plate, providing only small isotropic strain as temperature cools down. The

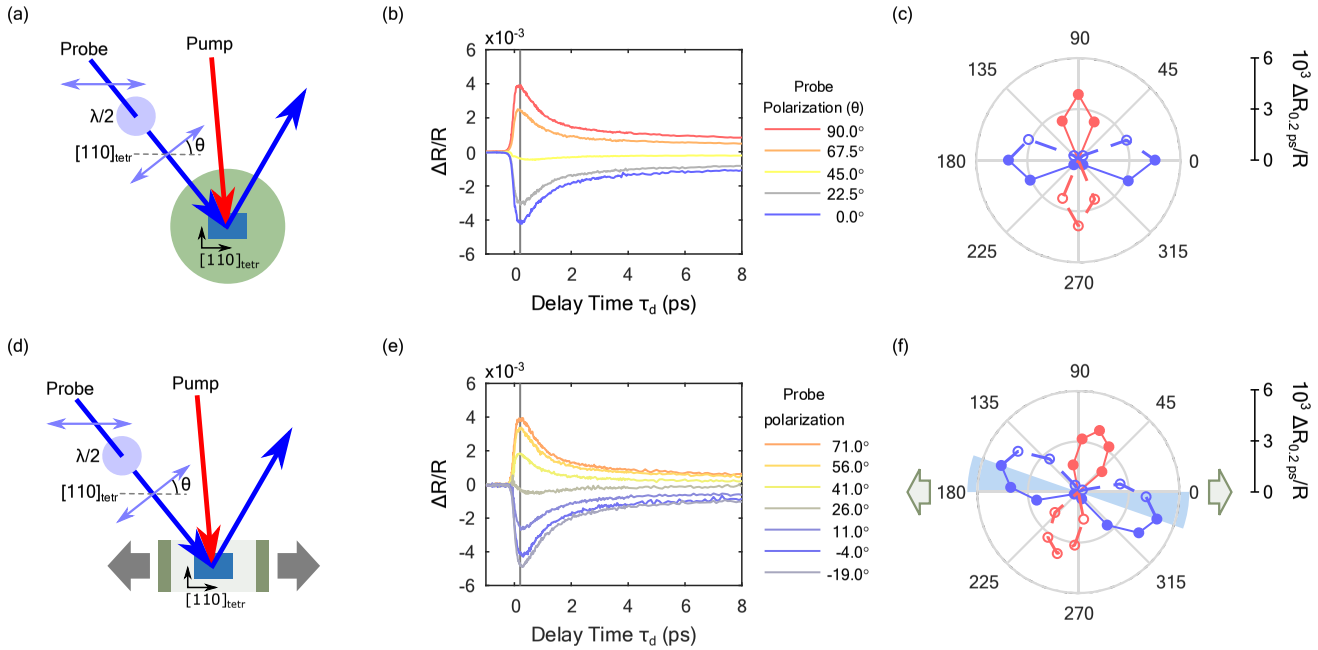

Figure 5.1: Strain dependent experiment on the photo-reflectivity performed at $Ba(Fe_{0.955}Co_{0.045})_2As_2$ single crystals. Experimental schematics (a) of the isotropic strain condition and (d) of the uniaxial-strain condition. Probe polarization dependent evolution of the photo-reflectivity $\Delta R/R$ is measured at 30 K as a function of delay time τ_d (b) under isotropic strain and (e) under uniaxial-strain. The polling axis of the piezo-stack is aligned to be parallel to $[110]_{\text{tetr}}$ crystal orientation. Polar axis plot of the photo-reflectivity measured at $\tau_d = 0.2$ ps as a function of the probe polarization (c) under isotropic strain and (f) under uniaxial-strain. Fluences are set to be 120 μJ/cm^2 for the incident pump and 20 μJ/cm^2 for the incident probe at the experiment under the isotropic strain, and 39 μJ/cm^2 for the incident pump and 1.2 μJ/cm^2 for the incident probe under the uniaxial-strain.

photo-reflectivity measured at 30 K exhibits a peak structure by the ultrafast pumping and it is followed by a recovery process of a picosecond relaxation time. As discussed in Chapter 3, the photo-reflectivity sensitively depends on the probe polarization while the rising and relaxation time scales do not. Polar-axis plot of the peak value measured at $\tau_d = 0.2$ ps clearly exhibits the broken C_4 symmetry along $[110]_{\text{tetr}}$, which corresponds to the B_{2g} nematicity. The results corroborate previous ultrafast investigations on the B_{2g} nematicity under isotropic-strain condition [Stojchevska et al., 2012, Patz et al., 2014, Luo et al., 2017, Liu et al., 2018].

Under the uniaxial-strain along $[110]_{\text{tetr}}$, the photo-reflectivity shows unexpected dependence on the probe polarization. The dynamics of the peak structure and its recovery in Fig. 5.1(e) are similar to the result under the isotropic-strain. In Fig. 5.1(f), however, the principal axis of the broken C_4 symmetry is rotated by about 20° from $[110]_{\text{tetr}}$. This implies the deviation from the B_{2g} nematic state. Note that the peculiar rotation does not depends on the measuring spot of the sample surface. About 20° rotation is uniformly appeared in the wide area of sample surface. Only its direction can be reversed when the same experiment is performed on another sample affixed to the piezo-stack. Note that the peculiar rotation is also not affected by the pump polarization.

The uniaxial-strain has been employed to provide a large single domain. The uniaxial-strain has been believed to simply detwin the crystal maintaining the B_{2g} nematicity although the applied strain may increase the nematicity.

It has never been expected that the rotation of the nematic response can be caused by the uniaxial-strain along $[110]_{\mathrm{tetr}}$ in the electron doped iron-pnictide. In heavily hole doped compound, on the other hand, there have been reports of B_{1g} nematicity. In a moderately hole doped case, furthermore, it is also reported the nearly isotropic nematic fluctuations due to the competition of B_{2g} and B_{1g} nematic states [Liu et al., 2019, Ishida et al., 2019]. Theoretical studies suggest that the competition of the two nematic orders is governed by the different spin alignments depending on the hole doping [Onari and Kontani, 2019, Borisov et al., 2019]. Therefore, one might expect that the rotation of nematicity observed in the photo-reflectivity under uniaxial-strain can be explained by a peculiar effect of the pump-induced photo-doped carriers, although the data on a copper plate does show the typical B_{2g} nematicity.

To disentangle the roles of the uniaxial-strain and the photo-doping in the nematicity rotation, we measured the reflectivity anisotropy, that is, the difference between reflectivity at two perpendicular polarizations $\delta R = R(\theta) - R(\theta + 90^{\circ})$ with and without photon pumping. For a sensitive reflectivity anisotropy measurement, we employed photo-elastic-modulator with a lock-in technique. Furthermore, we get rid of the geometric effect in the reflectivity anisotropy due to the non-perfect normal incidence of the probe beams by using a method described in Ref. [Kwak et al., 2019b]. Figure 5.2 shows the measured reflectivity anisotropy with and without photon pumping on the sample under the uniaxial-tensile-strain along $[110]_{\mathrm{tetr}}$. Equilibrium anisotropy without pumping δR^{eq} measured as a function of the incident probe polarization exhibits a

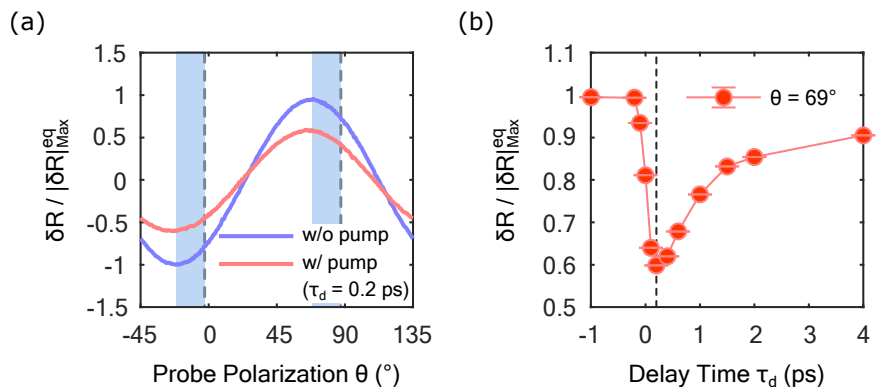

Figure 5.2: Reflectivity anisotropy of $Ba(Fe_{0.955}Co_{0.045})_2As_2$ is measured at 30 K under uniaxial-strain along $[110]_{tetr}$ using the method discussed in Chapter 4. The result is normalized by the maximum value of equilibrium anisotropy measured without pumping. (a) Reflectivity anisotropy $\delta R/|\delta R|^{eq}_{Max}$ measured as functions of θ in equilibrium state without pumping (blue solid line) and in non-equilibrium state at $\tau_d = 0.2$ ps (red solid line). The incident probe polarizations of $\theta = 0°$ and $\theta = 90°$ are parallel to the Fe-Fe bonding directions. (b) Time-transient reflectivity anisotropy $\delta R/|\delta R|^{eq}_{Max}$ as a function of delay time τ_d measured at the incident probe polarization of $\theta = 69°$. A dashed vertical line indicates $\tau_d = 0.2$ ps.

sinusoidal function of 180° period, implying the broken four-fold symmetry of the electronic structure. However, its phase is shifted by about 20° from the B_{2g} symmetry as displayed in Fig. 5.2(a). We note that the same amount of the phase shift is observed in the transient anisotropy change $\Delta(\delta R)/R$ after the ultrafast photo-excitation, but the sign is opposite to the case in equilibrium as displayed in Fig. 5.2(b). This implies that the ultrafast photo-excitation suppresses the nematic order rather than introduces any unexpected or exotic effect.

Delay time dependent evolution of the transient reflectivity anisotropy further confirms that the ultrafast pumping does not contribute to the 20° rotation of the broken four-fold symmetry. Figure 5.3(a) presents the time dependent evolution of the pump-induced change of the reflectivity anisotropy. As discussed with Fig. 5.2, the reflectivity anisotropy is suppressed after pumping and recovers as time goes on. During the onset as well as the recovery, the reflectivity anisotropy shows the same orientation shifted by 20° from the B_{2g} symmetry. In other words, there is no signature of pump-induced rotation of the nematic order.

Fluence dependent experiment also supports that the static nematic order is simply suppressed by the ultrafast photo-excitation. Figures 5.3(b) shows that the normalized transient reflectivity anisotropies measured at $\tau_d = 0.2$ ps at 41 and 1,000 μJ/cm^2 incident pump fluences coincide well with each other without any further rotation under stronger pump excitation. Figure 5.3(c) shows the maximum transient reflectivity anisotropy at $\tau_d = 0.2$ ps

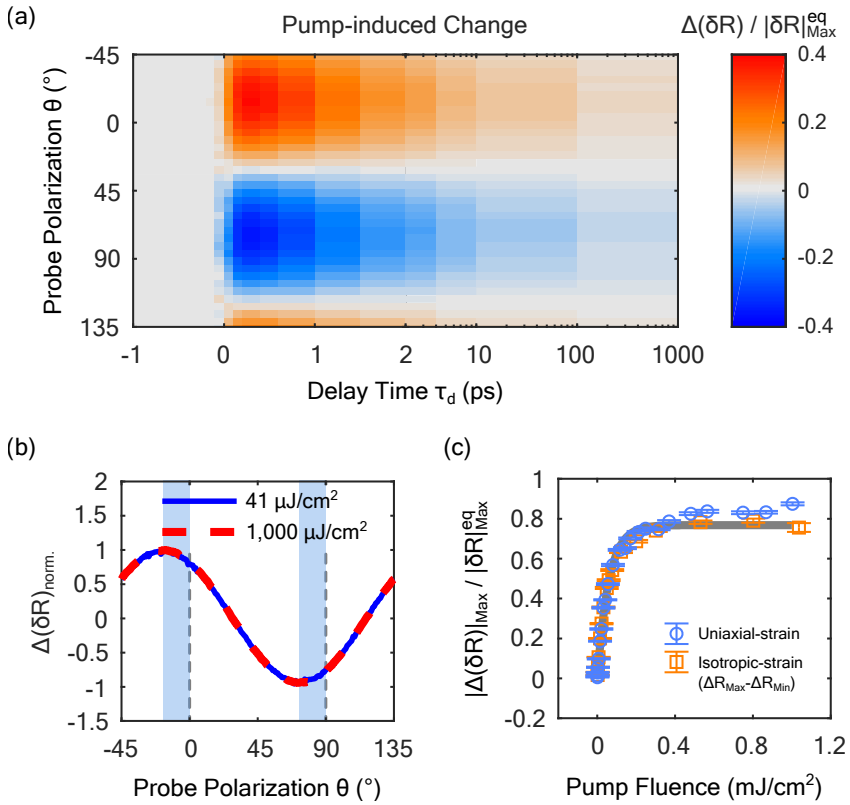

Figure 5.3: (a) Transient anisotropy change normalized by equilibrium anisotropy $\Delta(\delta R)/|\delta R|^{\rm eq}_{\rm Max}$ measured as a function of the incident probe polarization θ and the delay time τ_d at 30 K under uniaxial-strain. Incident fluences are set to be 41 μJ/cm^2 for pump and 5 μJ/cm^2 for probe. (b) Transient anisotropy change $\Delta(\delta R)/R$ measured as functions of the incident probe polarization at $\tau_d = 0.2$ ps with incident pump fluences of 41 μJ/cm^2 (blue solid line) and 1,000 μJ/cm^2 (red dashed line) respectively. They are normalized to the maximum values at each fluence conditions respectively. (c) Normalized transient anisotropy change by equilibrium anisotropy $|\Delta(\delta R)|_{\rm Max}/|\delta R|^{\rm eq}_{\rm Max}$ measured as a function of incident pump fluence. Isotropic-strain result (open circle) is obtained from difference between the maximum and the minimum values of the photo-reflectivity $\Delta R_{\rm Max} - \Delta R_{\rm Min}$ in Fig. 5.1(c). It is scaled to fit to the uniaxial-strain result (open square). A grey solid guide line is a simple saturation function of $|\Delta(\delta R)|_{\rm Max}/|\delta R|_{\rm Max} = A\left(1 - e^{-\Phi_{\rm sat}/\Phi}\right)$ where Φ is the incident pump fluence, $\Phi_{\rm sat} = 59$ μJ/cm^2, and $A = 0.77$.

normalized by the maximum reflectivity anisotropy in equilibrium. The fluence dependent evolution (open circle) fits well to the simple saturation model (grey solid line) with a saturation fluence $\Phi_{\mathrm{sat}} = 59\ \mu\mathrm{J/cm}^2$. Such a saturation behaviour suggests that a characteristic energy scale is required to suppress the nematic order [Lee et al., 2019]. It is interesting that the saturation characteristic is identical to the case of the small isotropic strain on a copper plate (open square). All our results consistently suggest that the ultrafast photo-excitation suppresses the reflectivity anisotropy due to the static nematic orders. Therefore, we conclude that the uniaxial-strain itself should be responsible for the peculiar rotation of the broken C_4 symmetry regardless of the ultrafast photo-excitation.

5.2.3 Applying uniaxial-strain by using piezoelectric-based apparatus

To clarify the role of uniaxial strain in the peculiar nematic rotation, we performed reflectivity anisotropy measurement of the sample affixed to the piezoelectric-based device as displayed in Fig. 5.4(a). For tensile-strain, the poled direction of the piezoelectric stack is aligned to be parallel to $[110]_{\mathrm{tetr}}$ and DC voltage of 150 V is applied to the two piezoelectric stacks located at the sides before cooling temperature. The apparatus provides a voltage-induced strain larger than affixing the sample directly to the piezoelectric stack because it utilizes the extension of the entire length of the piezoelectric stack. However, its maximum strain is expected to be much smaller than the

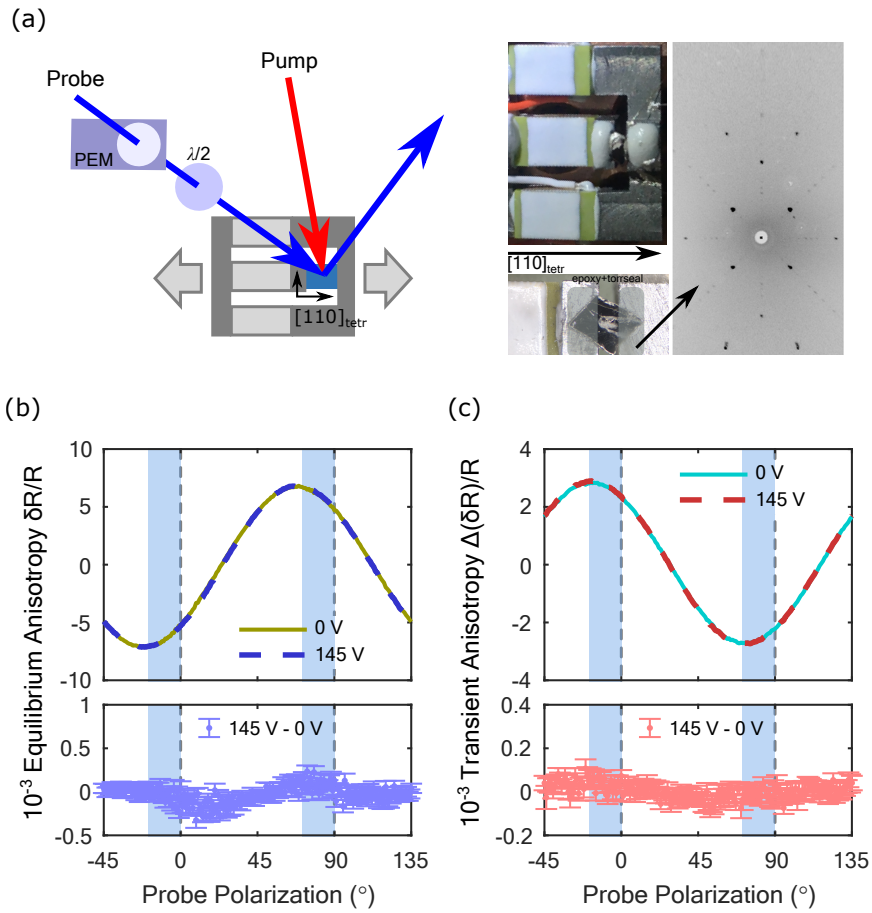

Figure 5.4: (a) Schematic diagram of time-resolved reflectivity anisotropy measurement on $Ba(Fe_{0.955}Co_{0045})_2As_2$ under uniaxial strain. The sample is affixed to the piezoelectric-based apparatus with silver-epoxy and torr-seal. Tensile-strain is applied along [110]tetr crystal orientation by applying DC voltage. (b) Equilibrium anisotropy $\delta R/R$ and (c) transient anisotropy $\Delta(\delta R)/R$ measured as functions of the incident probe polarization at 30 K with 0 V and 150 V DC voltage applied on the side piezoelectric stacks. The difference between 0 V and 150 V is displayed below panels respectively. The incident probe polarization of 0° is parallel to the crystal orientation of [110]tetr. Fluences are set to be 41 μJ/cm^2 for pump and 5 μJ/cm^2 for probe.

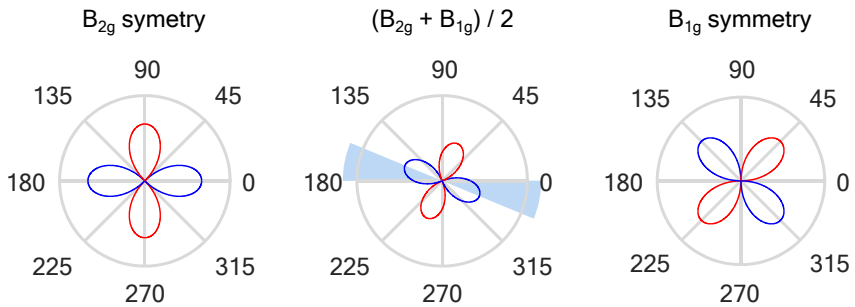

Figure 5.5: Polar axis plots of the numerically simulated sinusoidal functions. The red and blue colors indicate the positive and the negative signs respectively. The phase shift by 22.5° in the middle plot is simply obtained from average of the B2g symmetry (left) and the B1g symmetry (right).

thermal contraction induced uniaxial-tensile-strain.

Figure 5.4(b) displays equilibrium anisotropy $\Delta R/R$ measured as a function of the incident probe polarization at 30 K under the uniaxial strain along $[110]_{\mathrm{tetr}}$. The C_4 symmetry breaking is observed as a sinusoidal function of 180° period and its phase is still along 20° from $[110]_{\mathrm{tetr}}$ under 150 V DC and 0 V applied to the apparatus. This observation suggest that the peculiar rotation of the nematicity by 20° is introduced by fairly small tensile-strain and the strain-change is steeply saturates by the unintentional uniaxial-strain introduced by the differential thermal contraction between the sample and the apparatus. To exactly estimate the strength of the saturating strain, further systematic investigations are required.

5.2.4 Coexistence of B_{2g} and B_{1g} nematicity

Our result might seem counter intuitive and contradictory to previous studies claiming an enhanced nematic response under the uniaxial-strain as well as the detwinning effect. However, we find a possible coexistence of the B_{1g} nematic instability in $BaFe_2(As,P)_2$, a family compound of our system [Thewalt et al., 2018]. Thewalt *et al.* performed near-infrared pump-probe experiments and reported the C_4 symmetry breaking corresponding to the B_{2g} symmetry in the optimally isovalent substituted $BaFe_2(As,P)_2$, where the static nematic order is absent. They also performed careful micro Laue diffraction measurements to find out the local domain structure. Although they suggested that the ultrafast reflectivity showed the B_{2g} nematic response, the reported twin-domain boundaries are parallel to the Fe-Fe bonding, i.e. $[110]_{\mathrm{tetr}}$. In $Ba(Fe,Co)_2As_2$ and related materials, the nematic twin-domain boundary develops along the diagonal direction to the Fe-Fe bonding at the orthorhombic lattice transition. Therefore, the reported domain boundaries suggest that the principal orientation of the C_4 symmetry breaking should also be rotated by 45° from the usual orthorhombic axis parallel to the Fe-Fe bonding direction. Such 45° rotation of the domain boundary could be related to the B_{1g} nematic instability. The first principles calculations by Borisov *et al.* suggest that the key parameters for the manipulation of the B_{1g} nematicity are the c-axis strain and the number of Fe $3d$-electron [Borisov et al., 2019]. According to their result, a double stripe-type spin structure, responsible for the B_{1g} nematic state can become the ground state depending on the c-axis strain even with-

out hole doping. It suggests that the phosphorus substitution introduces the c-axis lattice contraction and therefore the B_{1g} nematic state can be realized.

Our observation of the intermediate nematic orientation under uniaxial-strain suggests that the B_{1g} instability could be enhanced by the uniaxial-strain in $Ba(Fe_{0.955},Co_{0.045})_2As_2$. The intermediate angle could be explained by the coexistence of B_{1g} and B_{2g} nematic responses. We note that it must be microscopic coexistence because the rotation angle of the 20° does not depend on the surface position. We speculate that the uniaxial-strain may enhance the spin fluctuation expected to play an important role for the B_{1g} nematicity in the heavily hole-doped systems [Onari and Kontani, 2019,Borisov et al., 2019]. However, it is not obvious how the uniaxial tensile-strain along $[110]_{\mathrm{tetr}}$ should lead to the mixed static nematic state. Unfortunately, the strain induced by the differential thermal contractions is much larger than the achievable strain by applying DC voltage on the piezo-stack [Thewalt et al., 2018, da Luz et al., 2009, Kuo, 2014]. The maximum stroke of the piezo-stack is 6.6 μm at 293 K, and decreases to 20 % at 77 K and to 5 % at 4 K. As a result, we have not noticed any change of the rotation angle within our experimental errorbar depending on the DC voltage applied to the piezoelectric stack. More theoretical and experimental efforts including systematic strain dependent measurements are strongly required.

5.3 Conclusion

In conclusion, we performed strain-dependent and time-resolved reflectometry experiments on $Ba(Fe_{0.955}Co_{0.045})_2As_2$ single crystals. We observed the peculiar rotation of the broken C_4 symmetry under the uniaxial strain along $[110]_{tetr}$. Our experimental results consistently demonstrate that the peculiar rotation is due to the uniaxial strain. The rotation of the nematic order by about 20° could be realized in the mixed state of the B_{2g} and the B_{1g} nematic orders. Our observations suggest that the uniaxial strain introduces unexpected instability to the nematic state in the electron-doped iron pnictide. Further studies are required to understand the complicated nematic instability in iron based superconductors.

6. Summary and Concluding Remarks

In this thesis, I present ultrafast studies on electronic nematicity of the electron-doped iron pnictide $Ba(Fe_{1-x}Co_x)_2As_2$ single crystals with x = 0 %, 4.5 %, 7.5 %, and 8.0 %. The measured photo-reflectivity are consisting of symmetric response independent on the probe polarization and asymmetric response dependent on the probe polarization. Temperature-dependent evolutions of the asymmetric photo-reflectivity show that nematic fluctuation strongly present near over wide range of doping even at the tetragonal phase, where the lattice C_4 symmetry is preserved. Fit analysis performed on both the asymmetric and the symmetric photo-reflectivities. The presence of SDW gap is observed at a ps relaxation process, implying that the fast asymmetric component corresponds to the spin-nematic fluctuations. The presence of coherent acoustic wave oscillations may support the assigning of the slow asymmetric component to the lattice nematic fluctuation.

I introduce a new experimental method to study the optical anisotropy by reflection experiment. Our new method makes it possible to distinguish the nematic optical anisotropy from the geometric anisotropy, which introduced by the non-zero angle of incidence. As a demonstration, the nematic anisotropy of $Ba(Fe_{0.955}Co_{0.045})_2As_2$ is measured at single crystal. Numerical simulations confirm that the experimentally observed data are highly reliable in conventional experimental environment. Successive time-resolved experiment on the nematic anisotropy assures that the ultrafast photo-excitation

simply suppresses the nematic anisotropy of the iron pnictides.

I performed strain-dependent and time-resolved reflectometry experiments on $Ba(Fe_{0.955}Co_{0.045})_2As_2$ single crystals. The peculiar rotation of the broken C_4 symmetry is observed under the uniaxial strain along $[110]_{tetr}$. The experimental results consistently demonstrate that the peculiar rotation occurs by the uniaxial strain. The rotation of the nematic order by about 20° suggest that the mixed state of the B_{2g} and the B_{1g} nematic orders could be realized by the uniaxial strain by introducing unexpected instability to the nematic state in the electron-doped iron pnictide. Further studies are required to understand the complicated nematic instability in iron based superconductors.

7. References

Bibliography

[Allen, 1987] Allen, P. B. (1987). *Phys. Rev. Lett.*, 59:1460.

[Averitt and Taylor, 2002] Averitt, R. D. and Taylor, A. J. (2002). *J. Phys. Condens. Matter*, 14:R1357.

[Beak et al., 2015] Beak, S.-H., Efremov, D. V., Ok, J. M., Kim, J. S., van den Brink, J., and Büchner, B. (2015). *Nat. Mater.*, 14:210.

[Beck et al., 2011] Beck, M., Klammer, M., Lang, S., Leiderer, P., Kabanov, V. V., Gol'tsman, G. N., and Demsar, J. (2011). *Phys. Rev. Lett.*, 107:177007.

[Borisov et al., 2019] Borisov, V., Fernandes, R. M., and Valentí, R. (2019). *Phys. Rev. Lett.*, 123:146402.

[Chu et al., 2010] Chu, J.-H., Analytis, J. G., Greve, K. D., Mcmahon, P. L., Islam, Z., Yamamoto, Y., and Fisher, I. R. (2010). *Science*, 329:824.

[Chubukov, 2012] Chubukov, A. (2012). *Annu. Rev. Condens. Matter Phys.*, 3:57.

[da Luz et al., 2009] da Luz, M. S., Neumeier, J. J., Bollinger, R. K., Sefat, A. S., McGuire, M. A., Jin, R., Sales, B. C., and Mandrus, D. (2009). *Phys. Rev. B*, 79:214505.

[Daou et al., 2010] Daou, R., Chang, J., LeBoeuf, D., Cyr-Choinière, O., Laliberté, F., Doiron-Leyraud, N., Ramshaw, B. J., Liang, R., Bonn, D. A., Hardy, W. N., and Taillefer, L. (2010). *Nature (London)*, 463:519–522.

[Demsar et al., 2003] Demsar, J., Averitt, R. D., Taylor, A. J., Kabanov, V. V., Kang, W. N., Kim, H. J., Choi, E. M., and Lee, S. I. (2003). *Phys. Rev. Lett.*, 91:267002.

[Gallais et al., 2013] Gallais, Y., Fernandes, R. M., Paul, I., Chauviére, L., YangM.-A., Y.-X., Méasson, Cazayous, M., Sacuto, A., Colson, D., and Forget, A. (2013). *Phys. Rev. Lett.*, 111:267001.

[Gallais and Paul, 2016] Gallais, Y. and Paul, I. (2016). *C. R. Physique*, 17:113.

[Gerber et al., 2015] Gerber, S., Kim, K. W., Zhang, Y., Zhu, D., Plonka, N., Yi, M., Dakovski, G. L., Leuenberger, D., Kirchmann, P., and *et al.*, R. G. M. (2015). *Nat. Commun.*, 6:7377.

[Gerber et al., 2017] Gerber, S., Yang, S.-L., Zhu, D., Soifer, H., Sobota, J. A., Rebec, S., Lee, J. J., Jia, T., Moritz, B., and *et al.*, C. J. (2017). *Science*, 357:71.

[Giannetti et al., 2016] Giannetti, C., Capone, M., Fausti, D., Fabrizio, M., Parmigiani, F., and Mihailovic, D. (2016). *Adv. Phys.*, 65:58.

[Graham and Lee, 2011] Graham, J. W. and Lee, J. K. (2011). In *30th URSI General Assembly and Scientific Symposium, Istanbul, Turky.*

[Groeneveld et al., 1995] Groeneveld, R. H. M., Sprik, R., and Lagendijk, A. (1995). *Phys. Rev. B*, 51:11433.

[He et al., 2017] He, M., Wang, L., Ahn, F., Hardy, F., Wolf, T., Adelmann, P., Schmalian, J., Eremin, I., and Meingast, C. (2017). *Nat. Commun.*, 8:504.

[Hosoi et al., 2016] Hosoi, S., Matsuura, K., Ishida, K., Wang, H., Mizukami, Y., Watashige, T., Kasahara, S., Matsuda, Y., and Shibauchi, T. (2016). *Proc. Nat. Acad. Sci. U. S. A.*, 113:8139.

[Huh et al., 2019] Huh, S. S., Seo, J. J., Kim, B. S., Cho, S. H., Jung, J. K., Kim, S., Koh, Y. Y., Kwon, C. I., Kim, J. S., and *et al.*, W. S. K. (2019). *arXiv:1903.08360v1.*

[Ikeda et al., 2018] Ikeda, M. S., Worasaran, T., Palmstrom, J. C., Straquadine, J. A. W., Walmsley, P., and Fisher, I. R. (2018). *Phys. Rev. B*, 98:245133.

[Ishida et al., 2019] Ishida, K., Tsujii, M., Hosoi, S., Mizukami, Y., Ishida, S., Iyo, A., Eisaki, H., Wolf, T., Grube, K., Löhneysen, H. v., Fernandes, R. M., and Shibauchi, T. (2019). *arXiv:1812.05267v2.*

[Kabanov et al., 1999] Kabanov, V. V., Demsar, J., Podobnik, B., and Mihailovic, D. (1999). *Phys. Rev. B*, 59:1497.

[Kasahara et al.,] Kasahara, S., Shi, H. J., Hashimoto, K., Tonegawa, S., Mizukami, Y., Shibauchi, T., Sugimoto, K., Fukuda, T., Terashima, T., Nevidomskyy, A. H., and Matsuda, Y.

[Keimer et al., 2015] Keimer, B., Kivelson, S. A., Norman, M. R., Uchida, S., and Zaanen, J. (2015). *Nature*, 518:179–186.

[Kim et al., 2012] Kim, K. W., Pashkin, A., Schäfer, H., Beyer, M., Porer, M., Wolf, T., Bernhard, C., Demsar, J., Huber, R., and Leitenstorfer, A. (2012). *Nat. Mater.*, 11:497.

[Kim et al., 2013] Kim, Y. K., Jung, W. S., Han, G. R., Choi, K.-Y., Chen, C.-C., Devereaux, T. P., Chainani, A., Miyawaki, J., Takata, Y., and *et al.*, Y. T. (2013). *Phys. Rev. Lett.*, 111:217001.

[Kretzschmar et al., 2016] Kretzschmar, F., Böhm, T., Karahasanovic, U., Muschler, B., Baum, A., Jost, D., Schmalian, J., Caprara, S., Grilli, M., and Castro, C. D. (2016). *Nat. Phys.*, 12:560.

[Kuo, 2014] Kuo, H.-H. (2014). *ELECTRONIC NEMATICITY IN IRON-BASED SUPERCONDUCTORS*. PhD thesis, Stanford University.

[Kuo et al., 2016] Kuo, H.-H., Chu, J.-H., Palmstrom, J. C., Kivelson, S. A., and Fisher, I. R. (2016). *Science*, 352:958.

[Kuo et al., 2013] Kuo, H.-H., Shapiro, M. C., Riggs, S. C., and Fisher, I. R. (2013). *Phys. rev. B*, 88:085113.

[Kusar et al., 2008] Kusar, P., Kabanov, V. V., Demsar, J., Mertelj, T., Sugai, S., and Mihailovic, D. (2008). *Phys. Rev. Lett.*, 101:227001.

[Kwak et al., 2019a] Kwak, I., Lee, M.-C., Park, B. C., Kim, C. H., Lee, B., Seo, C. W., Yamaura, J., Hiroi, Z., Noh, T. W., and Kim, K. W. (2019a). *Phys. Rev. B*, 100:144309.

[Kwak et al., 2019b] Kwak, I., Son, J., Lee, B., Wolf, T., Sohn, C. H., Noh, T. W., and Kim, K. W. (2019b). *arXiv:1911.12920v1.*

[Lee, 2019] Lee, M.-C. (2019). *Non-equilibrium Spectroscopic Studies on Coherent Phonon Oscillations in Transition Metal Compounds.* PhD thesis, Seoul National University.

[Lee et al., 2019] Lee, Y., Kwak, I., Lee, M.-C., Seo, C., Kim, Y., Wolf, T., Noh, T. W., and Kim, K. W. (2019). *submitted to Phys. Status Solidi Rapid Res. Lett.*

[Lisowski et al., 2005] Lisowski, M., Loukakos, P. A., Melnikov, A., Radu, I., Ungureanu, L., Wolf, M., and Bovensiepen, U. (2005). *Phys. Rev. Lett.*, 95:137402.

[Liu et al., 2018] Liu, S., Zhang, C., Deng, Q., Wen, H.-H., Li, J.-X., Chia, E. E. M., Wang, X., and Xiao, M. (2018). *Phys. Rev. B*, 97:020505.

[Liu et al., 2019] Liu, X., Tao, R., Ren, M., Chen, W., Yao, Q., Wolf, T., Yan, Y., Zhang, T., and Feng, D. (2019). *Nat. Commun.*, 10:1039.

[Liu et al., 2016] Liu, Z., Gu, Y., Zhang, W., Gong, D., Zhang, W., Xie, T., Lu, X., Ma, X., Zhang, X., Zhang, R., Luo, H., and Li, S. (2016). *Phys. Rev. Lett.*, 117:157002.

[Luo et al., 2017] Luo, C., Cheng, P. C., Wang, S.-H., Chiang, J.-C., Lin, J.-Y., Wu, K.-H., Juang, J.-Y., Chareev, D. A., Volkova, O. S., and Vasiliev, A. N. (2017). *npj Quantum Mater.*, 2:32.

[Malinowski et al., 2019] Malinowski, P., Jiang, Q., Sanchez, J., Liu, Z., Mutch, J., Went, P., Liu, J., Ryan, P., Kim, J.-W., and Chu, J.-H. (2019). *arXiv:1911.03390v1.*

[Mandrus et al., 2001] Mandrus, D., Thompson, J. R., Gaal, R., Forro, L., Bryan, J. C., Chakoumakos, B. C., Woods, L. M., Sales, B. C., Fishman, R. S., and Keppens, V. (2001). *Phys. Rev. B*, 63:195104.

[Moon et al., 2013] Moon, S. J., Schafgans, A. A., Tanatar, M. A., Prozorov, R., Thaler, A., Canfield, P. C., Sefat, A. S., Mandrus, D., and Basov, D. N. (2013). *Phys. Rev. Lett.*, 110:097003.

[Nakajima et al., 2012] Nakajima, M., Ishida, S., Tomioka, Y., Kihou, K., Lee, C. H., Iyo, A., Ito, T., Kakeshita, T., Eisaki, H., and Uchida, S. (2012). *Phys. Rev. Lett.*, 109:217003.

[Okazaki et al., 2011] Okazaki, R., Shibauchi, T., Shi, H. J., Haga, Y., Matsuda, T. D., Yamamoto, E., Onuki, Y., Ikeda, H., and Matsuda, Y. (2011). *Science*, 331:439–442.

[Onari and Kontani, 2019] Onari, S. and Kontani, H. (2019). *Phys. Rev. B*, 100:020507(R).

[Oppermann et al., 2019] Oppermann, M., Bauer, B., Rossi, T., Zinna, F., Helbing, J., Lacour, J., and Chergui, M. (2019). *Optica*, 6:56–60.

[Paglione and Greene, 2010] Paglione, J. and Greene, R. L. (2010). *Nat. Phys.*, 6:645.

[Patz et al., 2014] Patz, A., Li, T., Ran, S., Fernandes, R. M., Schmalian, J., Bud'ko, S. L., Canfield, P. C., Perakis, I. E., and Wang, J. (2014). *Nat. Commun.*, 5:3229.

[Perfetti et al., 2007] Perfetti, L., Loukakos, P. A., Lisowski, M., Bovensiepen, U., Eisaki, H., and Wolf, M. (2007). *Phys. Rev. Lett.*, 99:197001.

[Pfau et al., 2019] Pfau, H., Rotundu, C. R., Palmstrom, J. C., Chen, S. D., Hashimoto, M., Lu, D., Kemper, A. F., Fisher, I. R., and Shen, Z.-X. (2019). *Phys. Rev. B*, 99:035118.

[Riggs et al., 2015] Riggs, S. C., Shapiro, M. C., Maharaj, A. V., Raghu, S., Bauer, E. D., Baumbach, R. E., Giraldo-Gallo, P., Wartenbe, M., and Fisher, I. R. (2015). *Nat. Commun.*, 6:6425.

[Ronning et al., 2017] Ronning, F., Helm, T., Shirer, K. R., Bachmann, M. D., Balicas, L., Chan, M. K., Ramshaw, B. J., McDonald, R. D., Balakirev, F. F., Jaime, M., Bauer, E. D., and Moll, P. J. W. (2017). *Nature*, 548:313–317.

[Sato et al., 2017] Sato, Y., Kasahara, S., Murayama, H., Kasahara, Y., Moon, E.-G., Nishizaki, T., Loew, T., Porras, J., Keimer, B., Shibauchi, T., and Matsuda, Y. (2017). *Nat. Phys.*, 13:1074.

[Shapiro et al., 2016] Shapiro, M. C., Hristov, A. T., Palmstrom, J. C., Chu, J.-H., and Fisher, I. R. (2016). *Rev. Sci. Instrum.*, 87:063902.

[Shibauchi et al., 2014] Shibauchi, T., Carrington, A., and Matsuda, Y. (2014). *Annu. Rev. Condens. Matter Phys.*, 5:113.

[Shimojima et al., 2019] Shimojima, T., Suzuki, Y., Nakamura, A., Mitsuishi, N., Kasahara, S., Shibauchi, T., Matsuda, Y., Ishida, Y., Shin, S., and Ishizaka, K. (2019). *Nat. Commun.*, 10:1946.

[Si and Steglich, 2010] Si, Q. and Steglich, F. (2010). *Science*, 329:1161–1166.

[Sohn et al., 2015] Sohn, C. H., Jeong, H., Jin, H., Kim, S., Sandilands, L. J., Park, H. J., Kim, K. W., Moon, S. J., Cho, D.-Y., Yamaura, J., Hiroi, Z., and Noh, T. W. (2015). *Phys. Rev. Lett.*, 115:266402.

[Stojchevska et al., 2012] Stojchevska, L., Mertelj, T., Chu, J.-H., Fisher, I. R., and Mihailovic, D. (2012). *Phys. Rev. B*, 86:024519.

[Sun et al., 2019] Sun, Y., Kittaka, S., Sakakibara, T., Machida, K., Wang, J., Wen, J., Xing, X., Shi, Z., and Tamegai, T. (2019). *Phys. Rev. Lett.*, 123:027002.

[Tam et al., 2017] Tam, D. W., Song, Y., Man, H., Cheung, S. C., Yin, Z., Lu, X., Wang, W., Frandsen, B. A., Liu, L., and *et al.*, Z. G. (2017). *Phys. Rev. B*, 95:060505(R).

[Tanatar et al., 2010] Tanatar, M. A., Blomberg, E. C., Kreyssig, A., Kim, M. G., Ni, N., Thaler, A., Bud'ko, S. L., Canfield, P. C., Goldman, A. I., Mazin, I. I., and Prozorov, R. (2010). *Phys. Rev. B*, 81:184508.

[Thewalt et al., 2018] Thewalt, E., Hayes, I. M., Hinton, J. P., Little, A., Patankar, S., Wu, L., Helm, T., Stan, C. V., Tamura, N., Analytis, J. G., and Orenstein, J. (2018). *Phys. Rev. Lett.*, 121:027001.

[Thomsen et al., 1986] Thomsen, C., Grahn, H. T., Maris, H. J., and Tauc, J. (1986). *Phys. Rev. B*, 34:4129.

[Tomić et al., 2013] Tomić, M., Jeschke, H. O., Fernandes, R. M., and Valentí, R. (2013). *Phys. Rev. B*, 87:174503.

[Tomić et al., 2012] Tomić, M., Valentí, R., and Jeschke, H. O. (2012). *Phys. Rev. B*, 85:094105.

[Tros and Woutersen, 2015] Tros, M. and Woutersen, S. (2015). *Opt. Lett.*, 40:2607–2609.

[Watanabe et al., 2009] Watanabe, S., Kondo, R., Kagoshima, S., and Shimano, R. (2009). *Phys. Rev. B*, 80:220408(R).

[Weightman et al., 2005] Weightman, P., Martin, D. S., Cole, R. J., and Farrell, T. (2005). *Reports on Progress in Physics*, 68:1251–1341.

[Willa et al., 2019] Willa, R., Fritz, M., and Schmalian, J. (2019). *Phys. Rev. B*, 100:085106.

[Yi et al., 2011] Yi, M., Lu, D., Chu, J.-H., Analytis, J. G., Sorini, A. P., Kemper, A. F., Moritz, B., Mo, S.-K., Moore, R. G., Hashimoto, M., Lee, W.-S., Hussain, Z., Devereaux, T. P., Fisher, I. R., and Shen, Z.-X. (2011). *Proc. Nat. Acad. Sci. U. S. A.*, 108:6878–6883.

[Yi et al., 2014] Yi, M., Zhang, Y., Liu, Z.-K., Ding, X., Chu, J.-H., Kemper, A. F., Plonka, N., Moritz, B., Hashimoto, M., Mo, S.-K., Hussain, Z., Devereaux, T. P., Fisher, I. R., Wen, H. H., Shen, Z.-X., and Lu, D. H. (2014). *Nature Communications*, 5:3711.

[Zimmermann et al., 1991] Zimmermann, W., Brandt, E. H., Bauer, M., Seider, E., and Genzel, L. (1991). *Physica C*, 183:99.

8. Appendix

8.1 Effective-temperature model

In this chapter, I briefly introduces the effective-temperature model, which provides one of the simplest picture for understanding non-equilibrium dynamics of the correlated electronic systems. This discussion is a part of a publication [Kwak et al., 2019a].

Figure 8.1 schematically displays the relaxation process based on the effective-

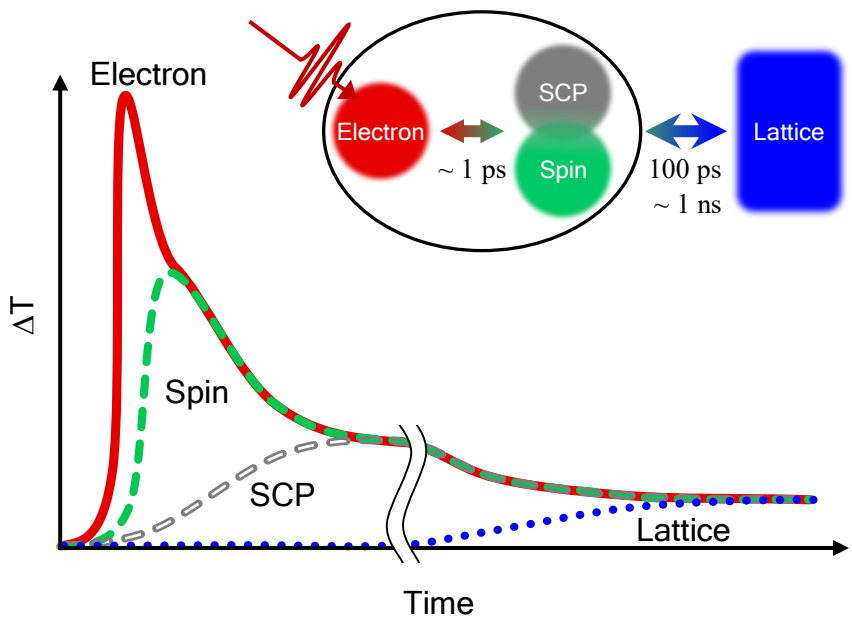

Figure 8.1: Schematic diagrams of the relaxation dynamics in terms of the effective-temperatures of the subsystems. Colored lines indicate the effective-temperature changes of the electron (solid line), spin (filled dashed line), strongly coupled phonon (SCP, open dashed line), and total lattice (dotted line) subsystems. This figure has been reproduced from [Kwak et al., 2019a].

temperatures including the electron (T_E), strongly coupled phonon (T_{SCP}), spin (T_S), and total lattice (T_L) subsystems. Hot electrons are generated in the excited states by the ultrafast pump excitation, thus elevating T_E. Then, the elevated T_E cools down by dissipating excess energy to the other subsystems. The scattering by the strongly coupled phonons (SCPs) is usually the most effective cooling channel, which dominates the sub-picosecond (ps) dynamics [Allen, 1987, Groeneveld et al., 1995, Perfetti et al., 2007, Giannetti et al., 2016, Averitt and Taylor, 2002]. In the strongly correlated materials, this scattering process is able to be modified by the magnetic order, introducing the spin subsystem into the ps dynamics [Averitt and Taylor, 2002, Lisowski et al., 2005, Watanabe et al., 2009, Patz et al., 2014]. It is crucial to investigate such ps dynamics for understanding the interplay between the electron, SCP, and spin subsystems.

In general, T_L remains close to the equilibrium temperature during the ps relaxation while the electron-SCP-spin subsystems reaches to the same effective temperature. The further heat-transfer takes place via the phonon-phonon or spin-phonon scattering over hundreds of ps or longer. After those scatterings, all the subsystems including the lattice, i.e. the entire phonon system, finally result in a quasi-equilibrium state at a slightly elevated temperature. The total system heating after the equilibration is much smaller than the initial heating of the electron subsystem, because the specific heat of the electron subsystem is only a small proportion of the total specific heat. Hence, the non-equilibrium electronic signal after cooling over hundreds of ps should become

negligible in comparison to the ps region.

8.2 Estimation of the maximum change of the effective temperature for $Cd_2Os_2O_7$

In this chapter, I describe the numerical estimation of the change in the lattice effective temperature by the pumping on $Cd_2Os_2O_7$ single crystal. This is a part of the publication [Kwak et al., 2019a].

8.2.1 Homogeneous absorption approximation

By assuming that an injected energy of a pump pulse (Q_{pump}) is homogenously absorbed in the measuring region, we estimate the maximum change of the effective-temperatures of the electron ($\Delta T_E^{\mathrm{hom}}$) and the lattice ($\Delta T_L^{\mathrm{hom}}$). To estimate ΔT_L^{hom}, we employed the value of heat capacity C_P of $Cd_2Os_2O_7$ single crystal from [Mandrus et al., 2001]:

$$\Delta T_L^{\mathrm{hom}} = \frac{\Delta Q_{\mathrm{pump}}}{C_P}. \tag{8.1}$$

To estimate ΔT_E^{hom}, we calculate the Sommerfeld coefficient γ, the linear coefficient of electron heat capacity:

$$\gamma = \frac{\pi^2 m^* k_{\mathrm{B}}^2}{\hbar^2} \left(3\pi^2 n\right)^{-2/3} (nV_m) \leq 3.0 \text{ mJ}/\left(\text{mol}\cdot\text{K}^2\right), \tag{8.2}$$

where n is a carrier density, V_m is a molar volume, and m^* is an effective mass of an electron. To consider whole candidates of photo-excited carriers, we obtained n by integrating optical conductivity at equilibrium temperature $T_{\mathrm{eq}} = 225$ K from 0 eV to 1.55 eV photon energy [Sohn et al., 2015]:

$$n \leq \frac{8\pi m^*}{h} \int_0^{1.55 \text{ eV}} \sigma(\omega)\, d\omega, \tag{8.3}$$

$$\Delta Q_{\text{pump}} = \int_{T_{\text{eq}}}^{T_{\text{eq}}+\Delta T_E^{\text{hom}}} \gamma T dT$$
$$= \frac{\gamma}{2}\left(2T_{\text{eq}}\Delta T_E^{\text{hom}} + \left[\Delta T_E^{\text{hom}}\right]^2\right), \tag{8.4}$$

$$\Delta T_E^{\text{hom}} = T_{\text{eq}}\left(\sqrt{1+\frac{2\Delta Q_{\text{pump}}}{\gamma T_{\text{eq}}^2}} - 1\right). \tag{8.5}$$

8.2.2 Exponential absorption & heat propagation approximation along depth

The assumption of the homogeneous absorption is not appropriate for estimation of the heating effect on optical properties from the maximum change of effective-temperatures ($\Delta T_E^{\max}$ and $\Delta T_L^{\max}$). Although the absorption at the sample surface is regarded to be homogeneous, the absorption along depth is not. Since the electromagnetic wave is exponentially attenuated with propagation, we should account for this by using the penetration depth twice (entering and exiting of the probe beam) [Kusar et al., 2008]:

$$\Delta T^{\max}(\tau_d) = \frac{2}{\lambda}\int_0^{\infty} \Delta T(z,\tau_d)\exp\left(-\frac{2z}{\lambda}\right)dz, \tag{8.6}$$

$$\Delta T(z,\tau_d) = T(z,\tau_d) - T_{\text{eq}}, \tag{8.7}$$

where $T(z,\tau_d)$ is the temperature distribution function at depth z and at time τ_d after pumping, and λ is the optical penetration depth. The value of $\lambda = 38$ nm at 1.55 eV is measured by ellipsometer.

To simulate $T(z,\tau_d)$ in the ns time domain, we employed a simple 1D heat equation with a boundary condition of the optical absorption:

$$\frac{\partial T(z,\tau_d)}{\partial \tau_d} - \alpha\frac{\partial^2 T(z,\tau_d)}{\partial z^2} = 0, \tag{8.8}$$

$$T\left(z,0\right)=\Delta T^{\mathrm{hom}}\exp\left(-\frac{z}{\lambda}\right)+T_{\mathrm{eq}}, \tag{8.9}$$

where α is a thermal diffusivity. The values of α is employed from [Mandrus et al., 2001]. Although this model is not realistic in the non-equilibrium state, it provides us a simple estimation of the heating effect in the quasi-equilibrium state. By solving 1D heat equation Eqs. (8.8) and (8.9) numerically, we finally obtained ΔT_E^{max} and ΔT_L^{max} from Eq. (8.6):

$$\Delta T_E^{\mathrm{max}}\sim 333\ \mathrm{K}\ (\mathrm{at}\ \tau_d=0\ \mathrm{ns}), \tag{8.10}$$

$$\Delta T_L^{\mathrm{max}}\sim 1\ \mathrm{K}\ (\mathrm{at}\ \tau_d=1.8\ \mathrm{ns}). \tag{8.11}$$

8.3 Ultrafast dynamics of a 5d pyrochlore antiferromagnet $Cd_2Os_2O_7$

In this section, I briefly present the non-equilibrium dynamics of $Cd_2Os_2O_7$. This study is an example which will provide understanding based on the effective temperature model for non-equilibrium dynamics in the strongly correlated systems. This study is published as a regular article [Kwak et al., 2019a].

The 5d pyrochlore $Cd_2Os_2O_7$ is a prototype all-in-all-out (AIAO) antiferromagnetic material exhibiting the *Lifshitz* transition accompanied by MIT.

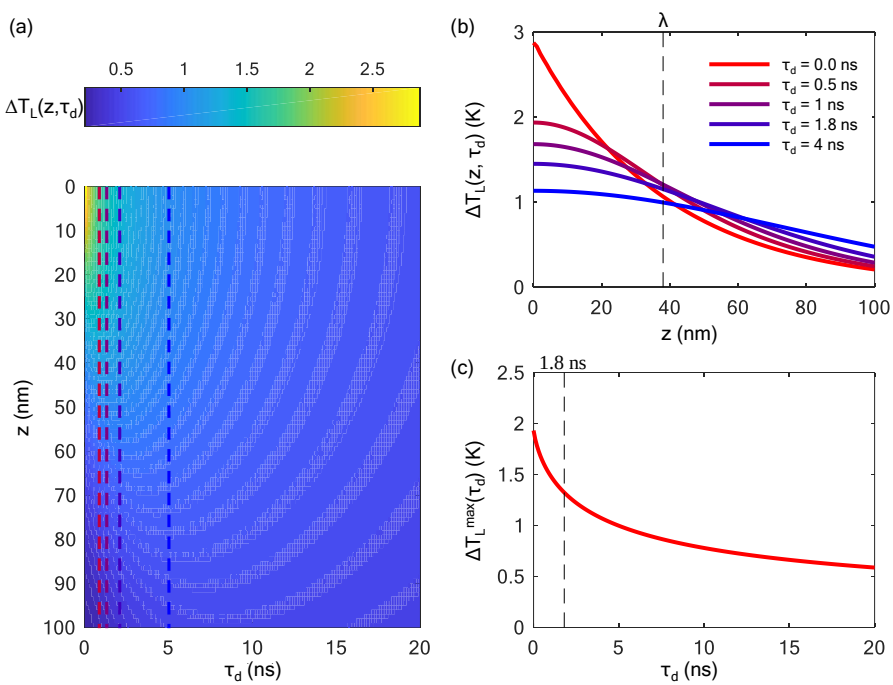

Figure 8.2: (a) Temperature distribution function $T_L(z, \tau_d)$ at 100 nm and 20 ns window. (b) Lattice temperature change distribution $\Delta T_L(z, \tau_d)$ at various time delay τ_d. (c) The lattice temperature change distribution $\Delta T_L(z, \tau_d)$ integrated over the depth. This figure has been reproduced from [Kwak et al., 2019a].

Because its resistivity increases abruptly below the antiferromagnetic transition temperature $T_N = 227$ K, the MIT is believed to be closely related to the magnetic order. Therefore, the system provides a good testbed to explore the temperature dependent evolution of various properties across the *Lifshitz* transition.

Figure 8.3 shows the temperature-dependent evolution of the photo-reflectivity

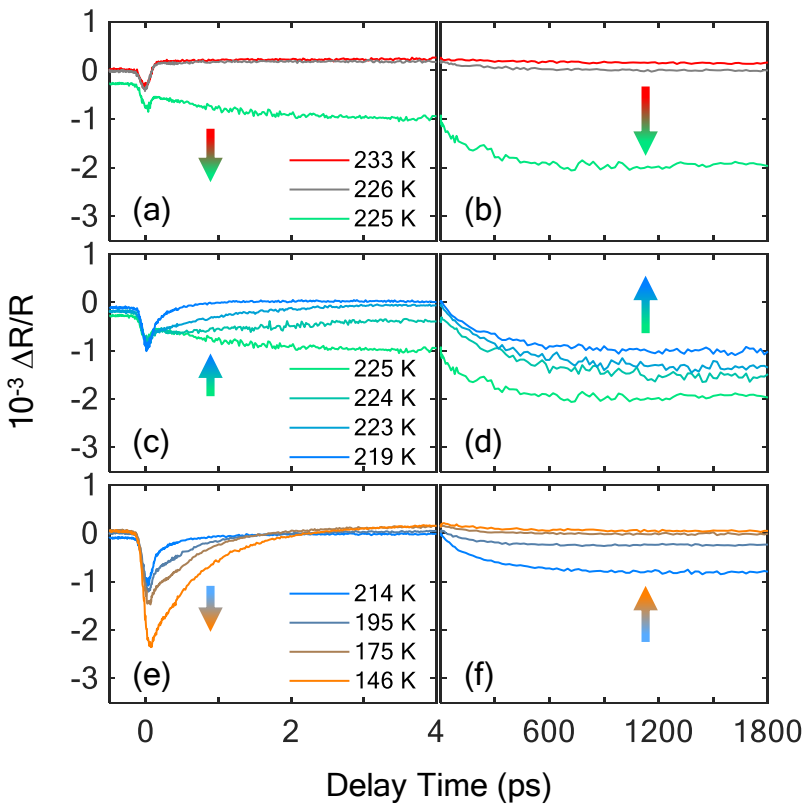

Figure 8.3: Photo-reflectivity $\Delta R/R$ in two temporal windows, spanning -0.5 – 4 ps (left panel), and 4 – 1,800 ps (right panel) over temperatures from 146 K to 233 K. This figure has been reproduced from [Kwak et al., 2019a].

$\Delta R/R$ measured at $Cd_2Os_2O_7$ single crystals grown by the chemical transport method. The ultrafast response above T_N is typical of a metal, which exhibits a sub-ps relaxation followed by a small offset [Figs. 8.3(a) and 8.3(b)]. Figures 8.3(c) and 8.3(e) show that additional, richly varied ps dynamics appears below T_N, and is much slower than the sub-ps dynamics that dominates above T_N. Unexpected is the result shown in Figs. 8.3(d) and 8.3(f) that the photo-reflectivity below T_N resurges over hundreds of ps. The photo-reflectivity in the nanosecond (ns) region is so unusually large that it becomes comparable to or even larger than the initial photo-reflectivity. The second law of thermodynamics state that the excess heat is transferred only from the lower temperature and to the higher temperature. In other words, effective temperatures such as T_S and T_E must monotonically decrease beyond 100 ps to reach the equilibrium state. Therefore, within the usual effective-temperature model, we cannot explain the huge resurgence in photo-reflectivity in the ns region in terms of T_S.

The simple thermodynamic simulation described in Chapter 8.2 shows that the pump excitation should heat up the electron subsystem by more than 300 K when the base temperature prior to pumping is close to T_N. After the heat has dissipated to all of the other subsystems, however, the temperature of the entire system is estimated to increase by only 1 K from the base temperature. In Fig. 8.4, we compare the photo-reflectivity at $t_d = 1.8$ ns ($\Delta R_{1.8\text{ns}}/R$) with the thermo-modulation of the reflectivity $(\partial R_{\text{eq}}/\partial T)/R_{\text{eq}}$. The good agreement between $\Delta R_{1.8\text{ns}}/R$ and $(\partial R_{\text{eq}}/\partial T)/R_{\text{eq}}$ suggests that the system in-

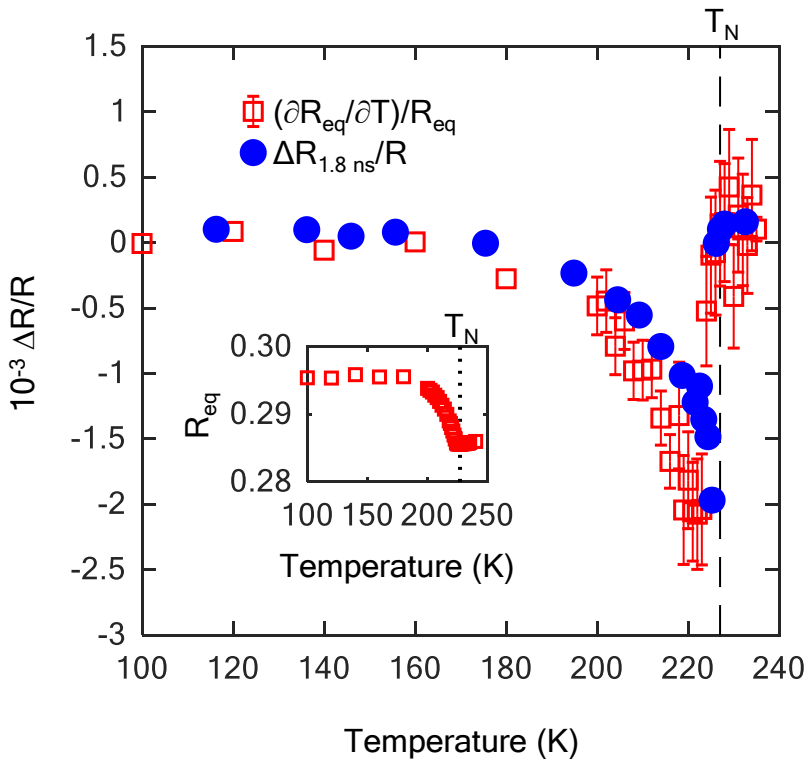

Figure 8.4: (Color online) Temperature-dependent evolution of $\Delta R/R$ (circles) measured at $t_d = 1.8$ ns and $(\partial R_{\rm eq}/\partial T)/R_{\rm eq}$ (squares) obtained from the equilibrium reflectivity $R_{\rm eq}$. Inset: The $R_{\rm eq}$ at 1.55 eV measured by spectroscopic ellipsometry at 20 K intervals from 100 to 200 K, and at 1 K intervals from 200 to 235 K. This figure has been reproduced from [Kwak et al., 2019a].

deed reaches a quasi-equilibrium state at $t_d = 1.8$ ns, where the temperature of all subsystems is slightly elevated by 1 K, as shown in Fig. 8.1. Therefore, the photo-reflectivity resurging over hundreds of picoseconds goes beyond the usual realm of the effective-temperature model.

8.4 Optical pump - THz probe spectroscopy setup

In this section, I schematically show optical pump - THz probe spectroscopy systems which I have established.

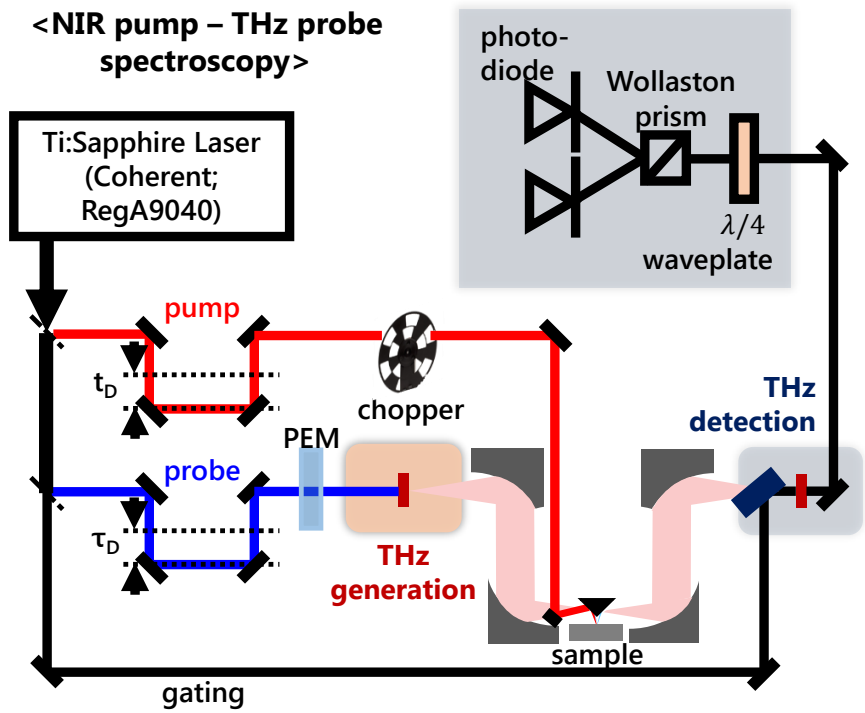

Figure 8.5: Schematic diagram of experimental set-up for optical pump - THz probe spectroscopy. This figure has been reproduced with the permission of [Lee, 2019].

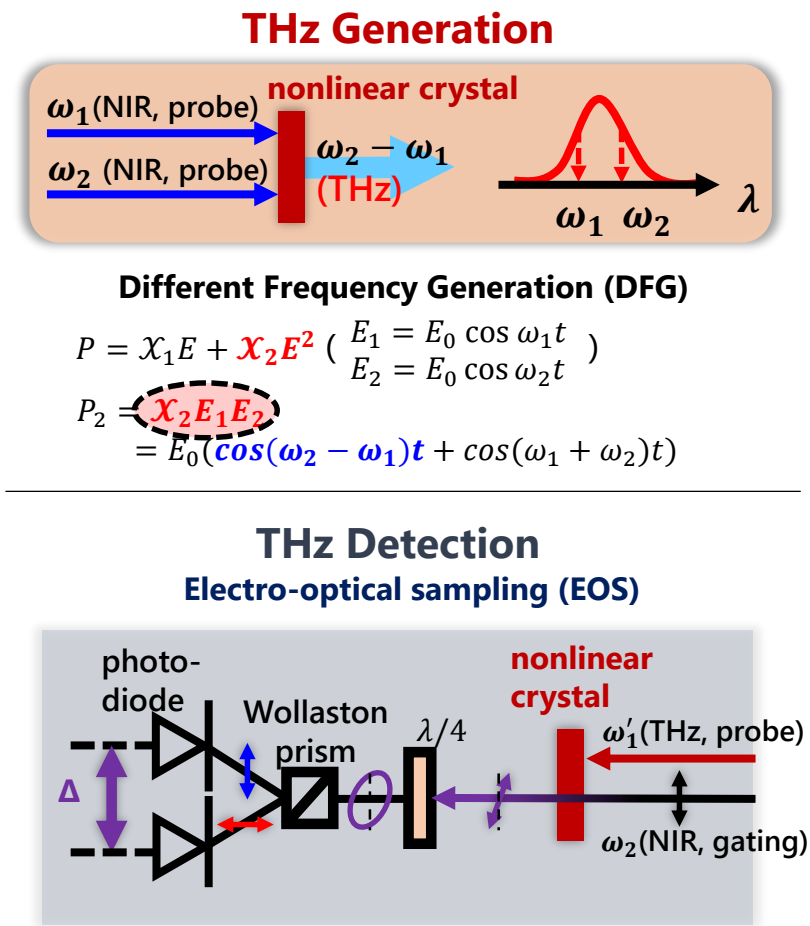

Figure 8.6: Generation and detection mechanism of THz lights by using second harmonic effects. This figure has been reproduced with permission of [Lee, 2019]

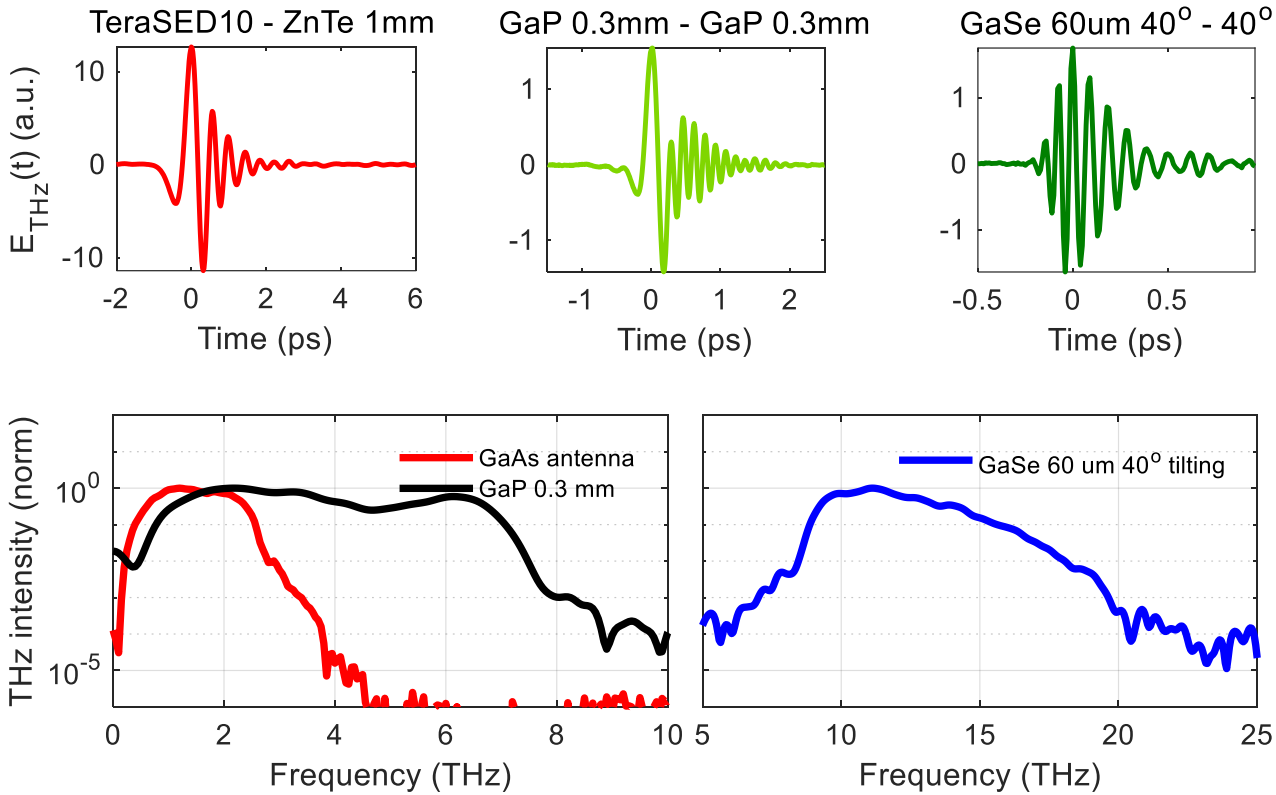

Figure 8.7: THz spectra obtained with the home-made THz spectroscopy equipment in IBS-CCES.

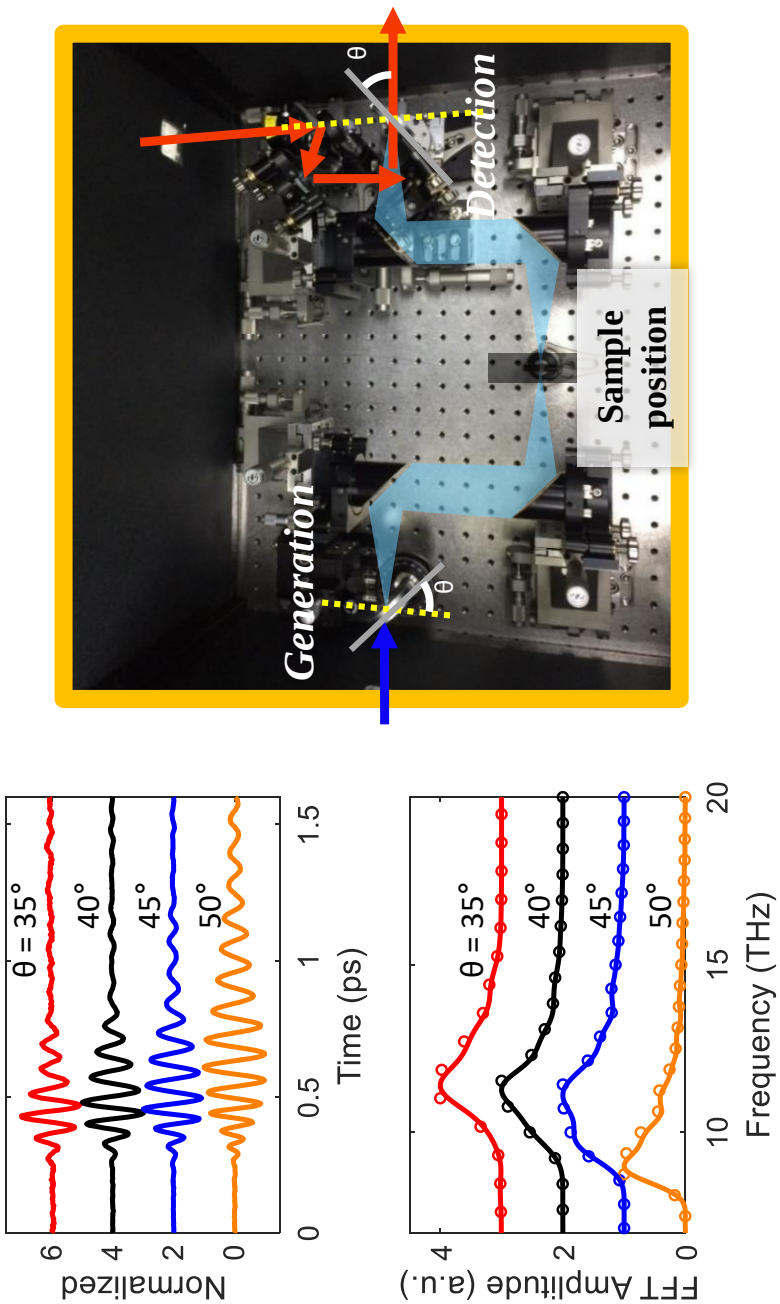

Figure 8.8: Demonstration of THz spectra tuning by rotating GaSe non-linear crystal of 60 μm thickness. This varies the angle of incidence of the generation beam and, therefore, the phase-matching condition changes. Note that the pulse duration of the generation beam is about 40 fs FWHM and bandwidth is 30 nm FWHM at 800 nm center frequency.

8.5 Optical pump - THz probe spectroscopy performed at $Ba_{0.6}K_{0.4}BiO_3$ superconducting film

In this section, I briefly show THz time-domain spectroscopy and optical-pump/THz-probe spectroscopy on $Ba_{0.6}K_{0.4}BiO_3$ superconducting film as demonstration of the home-made equipment.

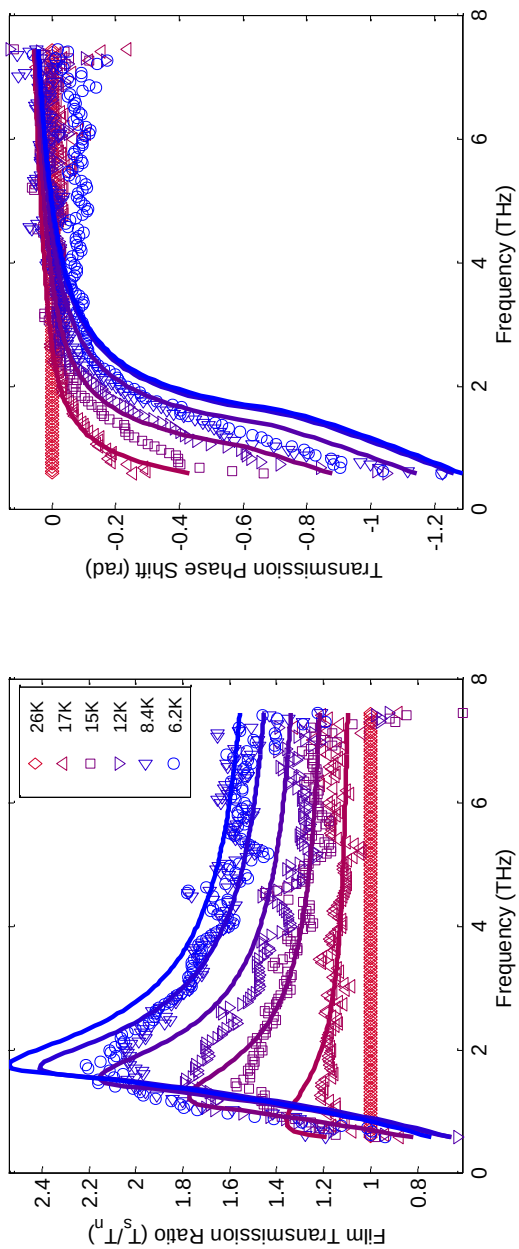

Figure 8.9: THz time-domain spectroscopy on the best quality $Ba_{0.6}K_{0.4}BiO_3$ superconducting film. Thickness of the film on a MgO substrate is 100 nm. Transmission spectra are measured at various temperature. Superconducting response is clearly observed in transmission spectra. The overall trend of T_S/T_N is understood by a single isotropic BCS gap dynamics. Thick solid lines are generated by simulation on transmission ratio with a single isotropic BCS gap [Zimmermann et al., 1991] using $T_C = 18$ K, $\Delta(0) = 3.43$ meV, and $\sigma_{DC} = 950\ \Omega^{-1}\text{cm}^{-1}$.

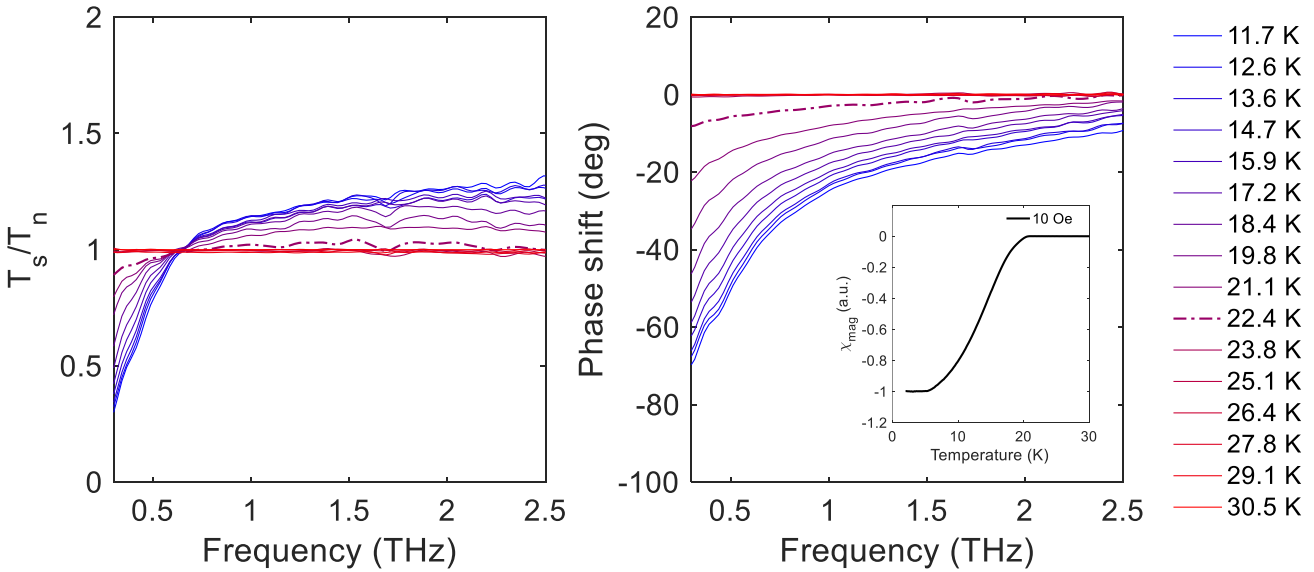

Figure 8.10: THz time-domain spectroscopy on a degraded $Ba_{0.6}K_{0.4}BiO_3$ superconducting film. Thickness of the film on a MgO substrate is 100 nm. Transmission spectra are measured at various temperature. The measured transmittivity spectra is not explained by isotropic single gap feature. Onset plot in a right panel exhibits the magnetic susceptibility data χ_m as a function of temperature. Broad transition in χ_m may be explained by continuous distribution of different Δ_{SC} size.

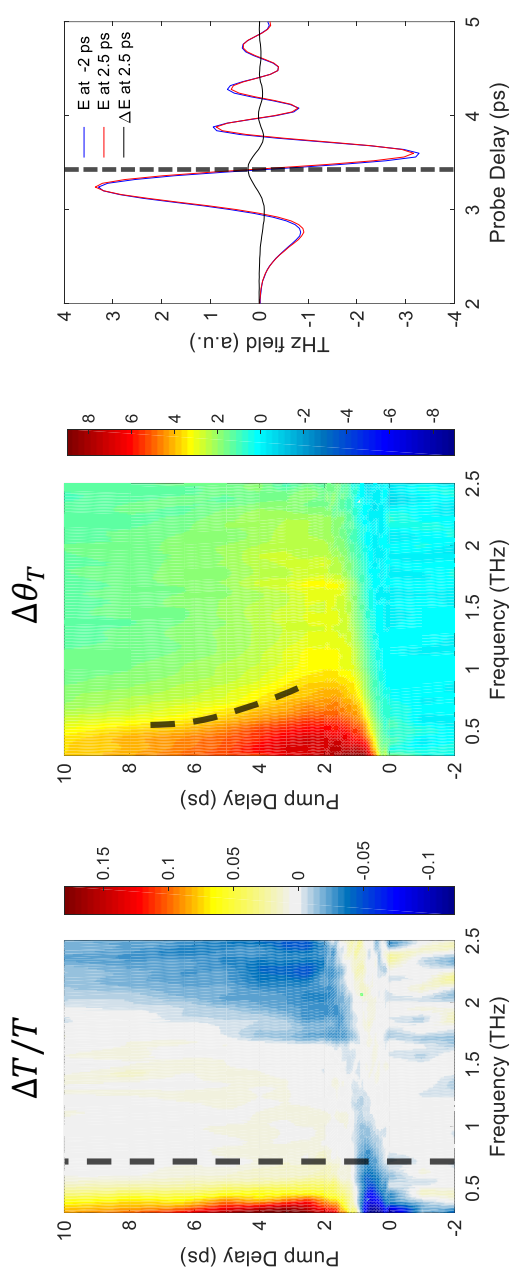

Figure 8.11: Optical-pump and THz-probe spectroscopy is performed on the degraded $Ba_{0.6}K_{0.4}BiO_3$ superconducting film performed at 11.7 K with 0.69 $\mu J/cm^2$ pump fluence. Fast relaxation is clearly observed in the transient change of transmission phase $\Delta\theta_T$. Pump induced signal results from phase change in THz electric field. It is consistent to temperature dependent evolution of the equilibrium transmission.

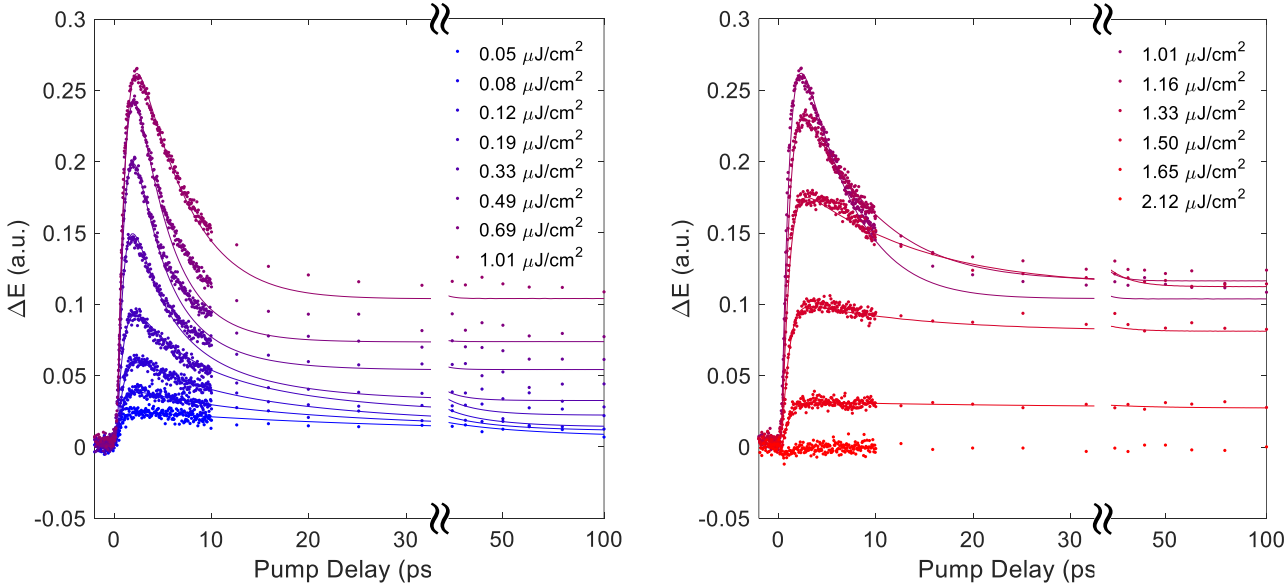

Figure 8.12: Fluence dependent optical-pump and THz-probe spectroscopy on the degraded $Ba_{0.6}K_{0.4}BiO_3$ superconducting film performed at 11.7 K with fixed probe delay where the change in the electricfield ΔE is the maximum. Phonon bottleneck process is dominant below 1 $\mu J/cm^2$ pump fluence. Above that, bi-particle recombination becomes dominant. Full depletion of SC state by the optical pump is observed at 2 $\mu J/cm^2$ pump fluence, fairly small value compared to other conventional superconductors [Demsar et al., 2003, Beck et al., 2011].

9. Publication List

9.1 Publications for this thesis

1. *Ultrafast polarimetric ivestigation of the nematic fluctuation in the electron-doped iron pnictide* $Ba(Fe_{1-x}Co_x)_2As_2$,
   Inho Kwak, Y. S. Lee, Min-Cheol Lee, C. W. Seo, Bumjoo Lee, Byung Cheol Park, T. Wolf, Tae Won Noh, and K. W. Kim,
   in preparation.

2. *Measurement of small reflectivity anisotropy in the nematic state and its non-equilibrium dynamics*
   Inho Kwak, Jaeseok Son, Bumjoo Lee, Thomas Wolf, Changhee Sohn, Tae Won Noh, and K. W. Kim,
   arXiv:1911.12920, *in preparation for regular article.*

3. *Rotation of reflectivity anisotropy due to uniaxial strain along* $[110]_{tetr}$ *in the electron-doped Fe-based superconductor* $Ba(Fe_{0.955}Co_{0.045})_2As_2$,
   Inho Kwak, Soon Sang Huh, Min-Cheol Lee, Younsik Kim, Bumjoo Lee, Y. S. Lee, C. W. Seo, Byung Cheol Park, T. Wolf, Changyoung Kim, Tae Won Noh, and K. W. Kim,
   in preparation.

9.2 Other publications

4. *Nematic fluctuations in optimally doped* $BaFe_{1.87}Co_{0.13}As_2$ observed in ultrafast photo-reflectivity,
   Yeong Seon Lee, **Inho Kwak**, Min-Cheol Lee, Choongwon Seo, Youngchan Kim, T. Wolf, T. W. Noh, K. W. Kim,
   Physica Status Solidi - Rapid Research Letters,
   https://doi.org/10.1002/pssr.201900584.

5. *Evidence of structural evolution in* Sr_2RhO_4 *studied by time-resolved optical reflectivity spectroscopy*,
   Min-Cheol Lee, **Inho Kwak**, Choong H. Kim, Bumjoo Lee, Byung Cheol Park, Junyoung Kwon, Wonshik Kyung, Changyoung Kim, Tae Won Noh, and Kyungwan Kim,
   Physical Review B **100**, 235139 (2019).

6. *Ultrafast dynamics in the Lifshitz-type 5d pyrochlore antiferromagnet* $Cd_2Os_2O_7$,
   Inho Kwak, Min-Cheol Lee, Byung Cheol Park, Choong H. Kim, Bumjoo Lee, C. W. Seo, J. Yamaura, Z. Hiroi, Tae Won Noh, and K. W. Kim,
   Physical Review B **100**, 144309 (2019).

7. *Strong spin-phonon coupling unveiled by coherent phonon oscillations in* Ca_2RuO_4,
   Min-Cheol Lee, Choong H. Kim, **Inho Kwak**, C. W. Seo, Changhee Sohn, F. Nakamura, C. Sow, Y. Maeno, E.-A. Kim, T. W. Noh, and K.

W. Kim,

Physical Review B **99**, 144306 (2019).

8. *Abnormal phase flip in the coherent phonon oscillations of* Ca_2RuO_4, Min-Cheol Lee, Choong H. Kim, **Inho Kwak**, J. Kim, S. Yoon, Byung Cheol Park, Bumjoo Lee, F. Nakamura, C. Sow, Y. Maeno, T. W. Noh, and K. W. Kim,

Physical Review B **98**, 161115(R) (2018).

10. Korean abstract

국문 초록

철계초전도체 $Ba(Fe_{1-x}Co_x)_2As_2$의 네마틱 상태에 대한 초고속 비평형 분광학 연구

곽인호
물리천문학부
서울대학교 대학원

이 논문은 고온 초전도와의 연관성으로 인해 많은 관심을 받고 있는 철계 초전도체의 네마틱 특성에 대한 근적외선 편분광 펌프-프로브 실험 연구를 논한다.

근적외선 편분광 펌프-프로브 실험은 코발트 도핑 $x = 0$ %, 4.5 %, 7.5 %, 8.0 %인 $Ba(Fe_{1-x}Co_x)_2As_2$ 단결정 시료들에 대해서 수행되었다. 측정된 광반사율은 프로브의 편광에 따라 변화를 보이는 비대칭 광반사율과 프로브 편광에 비의존적인 대칭 광반사율로 분리되어 분석되었다. 반대칭 광반사율의 온도에 따른 상세한 변화로부터 시료의 넓은 도핑 영역에 걸쳐 B_{2g} 대칭성을 갖는 네마틱 fluctuation이 존재함이 확인되었다. Spin-density-wave gap에 의한 준입자 동역학은 1 피코 초의 빠른 시간 범위에서 관찰되었으며, coherent acoustic wave oscillation은 대칭 광반사율의 10 피코 초 시간 범위에서 관측되었다. 이러한 측정 결과들은 반대칭 광반사율을 측정함으로써 스핀-네마

틱 fluctuation과 격자-네마틱 fluctuation 모두를 성공적으로 관찰할 수 있음을 보여준다.

네마틱 특성과 같이 작은 값의 이방성에 대한 광학적 측정 시도는 유한한 입사각 때문에 발생하는 s-편광 반사율과 p-편광 반사율 차이에 해당하는 기하학적 이방성에 의해서 어려움을 겪는 것이 보통이다. 본 연구에서는 이러한 문제를 해결함으로써 네마틱 특성 자체와 네마틱 정렬의 비평형 동역학까지 연구할 수 있게 만들어주는 새로운 실험 방법을 제안한다. 해당 방법의 유효성을 증명하고자 Fe-Fe 결합 방향으로 발달하는 B_{2g} 대칭성의 네마틱 상태를 갖는 $Ba(Fe_{1-x}Co_x)_2As_2$ 단결정에서 네마틱 특성에 의한 반사율 이방성을 측정하였다. 해당 실험 조건에 대해 수행한 수치 계산 결과로부터 본 연구에서 제안하는 새로운 측정 방식이 일반적인 실험 조건에서 매우 믿을만한 결과를 얻게 해줌을 확인하였다. 또한 해당 실험 방식을 사용하여 초고속 실험을 수행함으로써 네마틱 정렬이 초고속 펌프에 의해서 억제됨을 확인하였다.

마지막으로, 다양한 일방 변형 (uniaxial strain) 조건 아래에서 전형적인 B_{2g} 대칭성의 네마틱 특성을 보이는 $Ba(Fe_{0.955}Co_{0.045})_2As_2$ 단결정 시료에 대해 근적외선 편분광 펌프-프로브 실험을 수행하였다. 일반적으로 일방 외부 압력은 단일 도메인에서 네마틱 특성연구를 수행할 때에 사용된다. 하지만 본 연구를 통해 $[110]_{\mathrm{tetr}}$ 방향의 일방 변형 조건에서 수행된 광반사율 측정 결과 대칭성 깨짐 방향이 약 20도 만큼 돌아가는 것이 실험적으로 관찰되었다. 추가적으로 수행된 반사율 이방성 실험 결과 약 20도 정도의 독특한 회전은 일방 변형에 의해 유도됨이 확실시 되었다. 이와 같은 연구 결과는 코발트 도핑에 의해 전자가 추가된 철계초전도체에서도 B_{2g} 대칭성의 네마틱 상태와 B_{1g} 대칭성의 네마틱 상태가 microscopic하게 공존할 수 있음을 시사해

준다.

키워드: 초고속 분광학, 펌프-프로브 분광학, 강상관계물질, 초전도, 철계초전도체, 네마틱 정렬, 일방 변형

학번: 2014-21355